

Systematic Studies of Elliptic Flow Measurements in Au+Au Collisions at $\sqrt{s_{NN}} = 200$ GeV

S. Afanasiev,¹⁷ C. Aidala,⁷ N.N. Ajitanand,⁴⁴ Y. Akiba,^{38,39} J. Alexander,⁴⁴ A. Al-Jamel,³⁴ K. Aoki,^{23,38} L. Aphecetche,⁴⁶ R. Armendariz,³⁴ S.H. Aronson,³ R. Averbeck,⁴⁵ T.C. Awes,³⁵ B. Azmoun,³ V. Babintsev,¹⁴ A. Baldisseri,⁸ K.N. Barish,⁴ P.D. Barnes,²⁶ B. Bassalleck,³³ S. Bathe,⁴ S. Batsouli,⁷ V. Baublis,³⁷ F. Bauer,⁴ A. Bazilevsky,³ S. Belikov,^{3,16,*} R. Bennett,⁴⁵ Y. Berdnikov,⁴¹ M.T. Bjorndal,⁷ J.G. Boissevain,²⁶ H. Borel,⁸ K. Boyle,⁴⁵ M.L. Brooks,²⁶ D.S. Brown,³⁴ D. Bucher,³⁰ H. Buesching,³ V. Bumazhnov,¹⁴ G. Bunce,^{3,39} J.M. Burward-Hoy,²⁶ S. Butsyk,⁴⁵ S. Campbell,⁴⁵ J.-S. Chai,¹⁸ S. Chernichenko,¹⁴ J. Chiba,¹⁹ C.Y. Chi,⁷ M. Chiu,⁷ I.J. Choi,⁵³ T. Chujo,⁵⁰ V. Cianciolo,³⁵ C.R. Clevelin,¹² Y. Cobigo,⁸ B.A. Cole,⁷ M.P. Comets,³⁶ P. Constantin,¹⁶ M. Csanád,¹⁰ T. Csörgő,²⁰ T. Dahms,⁴⁵ K. Das,¹¹ G. David,³ H. Delagrange,⁴⁶ A. Denisov,¹⁴ D. d'Enterria,⁷ A. Deshpande,^{39,45} E.J. Desmond,³ O. Dietzsch,⁴² A. Dion,⁴⁵ J.L. Drachenberg,¹ O. Drapier,²⁴ A. Drees,⁴⁵ A.K. Dubey,⁵² A. Durum,¹⁴ V. Dzhordzhadze,⁴⁷ Y.V. Efremenko,³⁵ J. Egdemir,⁴⁵ A. Enokizono,¹³ H. En'yo,^{38,39} B. Espagnon,³⁶ S. Esumi,⁴⁹ D.E. Fields,^{33,39} F. Fleuret,²⁴ S.L. Fokin,²² B. Forestier,²⁷ Z. Fraenkel,^{52,*} J.E. Frantz,⁷ A. Franz,³ A.D. Frawley,¹¹ Y. Fukao,^{23,38} S.-Y. Fung,⁴ S. Gadrat,²⁷ F. Gastineau,⁴⁶ M. Germain,⁴⁶ A. Glenn,⁴⁷ M. Gonin,²⁴ J. Gosset,⁸ Y. Goto,^{38,39} R. Granier de Cassagnac,²⁴ N. Grau,¹⁶ S.V. Greene,⁵⁰ M. Grosse Perdekamp,^{15,39} T. Gunji,⁵ H.-Å. Gustafsson,²⁸ T. Hachiya,^{13,38} A. Hadj Henni,⁴⁶ J.S. Haggerty,³ M.N. Hagiwara,¹ H. Hamagaki,⁵ H. Harada,¹³ E.P. Hartouni,²⁵ K. Haruna,¹³ M. Harvey,³ E. Haslum,²⁸ K. Hasuko,³⁸ R. Hayano,⁵ M. Heffner,²⁵ T.K. Hemmick,⁴⁵ J.M. Heuser,³⁸ X. He,¹² H. Hiejima,¹⁵ J.C. Hill,¹⁶ R. Hobbs,³³ M. Holmes,⁵⁰ W. Holzmann,⁴⁴ K. Homma,¹³ B. Hong,²¹ T. Horaguchi,^{38,48} M.G. Hur,¹⁸ T. Ichihara,^{38,39} K. Imai,^{23,38} M. Inaba,⁴⁹ D. Isenhower,¹ L. Isenhower,¹ M. Ishihara,³⁸ T. Isobe,⁵ M. Issah,⁴⁴ A. Isupov,¹⁷ B.V. Jacak,^{45,†} J. Jia,⁷ J. Jin,⁷ O. Jinnouchi,³⁹ B.M. Johnson,³ K.S. Joo,³¹ D. Jouan,³⁶ F. Kajihara,^{5,38} S. Kametani,^{5,51} N. Kamihara,^{38,48} M. Kaneta,³⁹ J.H. Kang,⁵³ T. Kawagishi,⁴⁹ A.V. Kazantsev,²² S. Kelly,⁶ A. Khanzadeev,³⁷ D.J. Kim,⁵³ E. Kim,⁴³ Y.-S. Kim,¹⁸ E. Kinney,⁶ A. Kiss,¹⁰ E. Kistenev,³ A. Kiyomichi,³⁸ C. Klein-Boesing,³⁰ L. Kochenda,³⁷ V. Kochetkov,¹⁴ B. Komkov,³⁷ M. Konno,⁴⁹ D. Kotchetkov,⁴ A. Kozlov,⁵² P.J. Kroon,³ G.J. Kunde,²⁶ N. Kurihara,⁵ K. Kurita,^{40,38} M.J. Kweon,²¹ Y. Kwon,⁵³ G.S. Kyle,³⁴ R. Lacey,⁴⁴ J.G. Lajoie,¹⁶ A. Lebedev,¹⁶ Y. Le Bornec,³⁶ S. Leckey,⁴⁵ D.M. Lee,²⁶ M.K. Lee,⁵³ M.J. Leitch,²⁶ M.A.L. Leite,⁴² H. Lim,⁴³ A. Litvinenko,¹⁷ M.X. Liu,²⁶ X.H. Li,⁴ C.F. Maguire,⁵⁰ Y.I. Makdisi,³ A. Malakhov,¹⁷ M.D. Malik,³³ V.I. Manko,²² H. Masui,⁴⁹ F. Matathias,⁴⁵ M.C. McCain,¹⁵ P.L. McGaughey,²⁶ Y. Miake,⁴⁹ A. Mignerey,²⁹ T.E. Miller,⁵⁰ A. Milov,⁴⁵ S. Mioduszewski,³ G.C. Mishra,¹² J.T. Mitchell,³ D.P. Morrison,³ J.M. Moss,²⁶ T.V. Moukhanova,²² D. Mukhopadhyay,⁵⁰ J. Murata,^{40,38} S. Nagamiya,¹⁹ Y. Nagata,⁴⁹ J.L. Nagle,⁶ M. Naglis,⁵² T. Nakamura,¹³ J. Newby,²⁵ M. Nguyen,⁴⁵ B.E. Norman,²⁶ R. Nouicer,³ A.S. Nyanin,²² J. Nystrand,²⁸ E. O'Brien,³ C.A. Ogilvie,¹⁶ H. Ohnishi,³⁸ I.D. Ojha,⁵⁰ H. Okada,^{23,38} K. Okada,³⁹ O.O. Omiwade,¹ A. Oskarsson,²⁸ I. Otterlund,²⁸ K. Ozawa,⁵ R. Pak,³ D. Pal,⁵⁰ A.P.T. Palounek,²⁶ V. Pantuev,⁴⁵ V. Papavassiliou,³⁴ J. Park,⁴³ W.J. Park,²¹ S.F. Pate,³⁴ H. Pei,¹⁶ J.-C. Peng,¹⁵ H. Pereira,⁸ V. Peresedov,¹⁷ D.Yu. Peressounko,²² C. Pinkenburg,³ R.P. Pisani,³ M.L. Purschke,³ A.K. Purwar,⁴⁵ H. Qu,¹² J. Rak,¹⁶ I. Ravinovich,⁵² K.F. Read,^{35,47} M. Reuter,⁴⁵ K. Reygers,³⁰ V. Riabov,³⁷ Y. Riabov,³⁷ G. Roche,²⁷ A. Romana,^{24,*} M. Rosati,¹⁶ S.S.E. Rosendahl,²⁸ P. Rosnet,²⁷ P. Rukoyatkin,¹⁷ V.L. Rykov,³⁸ S.S. Ryu,⁵³ B. Sahlmueller,³⁰ N. Saito,^{23,38,39} T. Sakaguchi,^{5,51} S. Sakai,⁴⁹ V. Samsonov,³⁷ H.D. Sato,^{23,38} S. Sato,^{3,19,49} S. Sawada,¹⁹ V. Semenov,¹⁴ R. Seto,⁴ D. Sharma,⁵² T.K. Shea,³ I. Shein,¹⁴ T.-A. Shibata,^{38,48} K. Shigaki,¹³ M. Shimomura,⁴⁹ T. Shohjoh,⁴⁹ K. Shoji,^{23,38} A. Sickles,⁴⁵ C.L. Silva,⁴² D. Silvermyr,³⁵ K.S. Sim,²¹ C.P. Singh,² V. Singh,² S. Skutnik,¹⁶ W.C. Smith,¹ A. Soldatov,¹⁴ R.A. Soltz,²⁵ W.E. Sondheim,²⁶ S.P. Sorensen,⁴⁷ I.V. Sourikova,³ F. Staley,⁸ P.W. Stankus,³⁵ E. Stenlund,²⁸ M. Stepanov,³⁴ A. Ster,²⁰ S.P. Stoll,³ T. Sugitate,¹³ C. Suire,³⁶ J.P. Sullivan,²⁶ J. Sziklai,²⁰ T. Tabaru,³⁹ S. Takagi,⁴⁹ E.M. Takagui,⁴² A. Taketani,^{38,39} K.H. Tanaka,¹⁹ Y. Tanaka,³² K. Tanida,^{38,39} M.J. Tannenbaum,³ A. Taranenko,⁴⁴ P. Tarján,⁹ T.L. Thomas,³³ M. Togawa,^{23,38} J. Tojo,³⁸ H. Torii,³⁸ R.S. Towell,¹ V.-N. Tram,²⁴ I. Tserruya,⁵² Y. Tsuchimoto,^{13,38} S.K. Tuli,² H. Tydesjö,²⁸ N. Tyurin,¹⁴ C. Vale,¹⁶ H. Valle,⁵⁰ H.W. van Hecke,²⁶ J. Velkovska,⁵⁰ R. Vertesi,⁹ A.A. Vinogradov,²² E. Vznuzdaev,³⁷ M. Wagner,^{23,38} X.R. Wang,³⁴ Y. Watanabe,^{38,39} J. Wessels,³⁰ S.N. White,³ N. Willis,³⁶ D. Winter,⁷ C.L. Woody,³ M. Wysocki,⁶ W. Xie,^{4,39} A. Yanovich,¹⁴ S. Yokkaichi,^{38,39} G.R. Young,³⁵ I. Younus,³³ I.E. Yushmanov,²² W.A. Zajc,⁷ O. Zaudtke,³⁰ C. Zhang,⁷ J. Zimányi,^{20,*} and L. Zolin¹⁷

(PHENIX Collaboration)

¹Abilene Christian University, Abilene, TX 79699, U.S.

²Department of Physics, Banaras Hindu University, Varanasi 221005, India

³Brookhaven National Laboratory, Upton, NY 11973-5000, U.S.

⁴University of California - Riverside, Riverside, CA 92521, U.S.

- ⁵Center for Nuclear Study, Graduate School of Science, University of Tokyo, 7-3-1 Hongo, Bunkyo, Tokyo 113-0033, Japan
- ⁶University of Colorado, Boulder, CO 80309, U.S.
- ⁷Columbia University, New York, NY 10027 and Nevis Laboratories, Irvington, NY 10533, U.S.
- ⁸Dapnia, CEA Saclay, F-91191, Gif-sur-Yvette, France
- ⁹Debrecen University, H-4010 Debrecen, Egyetem tér 1, Hungary
- ¹⁰ELTE, Eötvös Loránd University, H - 1117 Budapest, Pázmány P. s. 1/A, Hungary
- ¹¹Florida State University, Tallahassee, FL 32306, U.S.
- ¹²Georgia State University, Atlanta, GA 30303, U.S.
- ¹³Hiroshima University, Kagamiyama, Higashi-Hiroshima 739-8526, Japan
- ¹⁴IHEP Protvino, State Research Center of Russian Federation, Institute for High Energy Physics, Protvino, 142281, Russia
- ¹⁵University of Illinois at Urbana-Champaign, Urbana, IL 61801, U.S.
- ¹⁶Iowa State University, Ames, IA 50011, U.S.
- ¹⁷Joint Institute for Nuclear Research, 141980 Dubna, Moscow Region, Russia
- ¹⁸KAERI, Cyclotron Application Laboratory, Seoul, Korea
- ¹⁹KEK, High Energy Accelerator Research Organization, Tsukuba, Ibaraki 305-0801, Japan
- ²⁰KFKI Research Institute for Particle and Nuclear Physics of the Hungarian Academy of Sciences (MTA KFKI RMKI), H-1525 Budapest 114, POBox 49, Budapest, Hungary
- ²¹Korea University, Seoul, 136-701, Korea
- ²²Russian Research Center “Kurchatov Institute”, Moscow, Russia
- ²³Kyoto University, Kyoto 606-8502, Japan
- ²⁴Laboratoire Leprince-Ringuet, Ecole Polytechnique, CNRS-IN2P3, Route de Saclay, F-91128, Palaiseau, France
- ²⁵Lawrence Livermore National Laboratory, Livermore, CA 94550, U.S.
- ²⁶Los Alamos National Laboratory, Los Alamos, NM 87545, U.S.
- ²⁷LPC, Université Blaise Pascal, CNRS-IN2P3, Clermont-Fd, 63177 Aubiere Cedex, France
- ²⁸Department of Physics, Lund University, Box 118, SE-221 00 Lund, Sweden
- ²⁹University of Maryland, College Park, MD 20742, U.S.
- ³⁰Institut für Kernphysik, University of Muenster, D-48149 Muenster, Germany
- ³¹Myongji University, Yongin, Kyonggido 449-728, Korea
- ³²Nagasaki Institute of Applied Science, Nagasaki-shi, Nagasaki 851-0193, Japan
- ³³University of New Mexico, Albuquerque, NM 87131, U.S.
- ³⁴New Mexico State University, Las Cruces, NM 88003, U.S.
- ³⁵Oak Ridge National Laboratory, Oak Ridge, TN 37831, U.S.
- ³⁶IPN-Orsay, Université Paris Sud, CNRS-IN2P3, BP1, F-91406, Orsay, France
- ³⁷PNPI, Petersburg Nuclear Physics Institute, Gatchina, Leningrad region, 188300, Russia
- ³⁸RIKEN Nishina Center for Accelerator-Based Science, Wako, Saitama 351-0198, JAPAN
- ³⁹RIKEN BNL Research Center, Brookhaven National Laboratory, Upton, NY 11973-5000, U.S.
- ⁴⁰Physics Department, Rikkyo University, 3-34-1 Nishi-Ikebukuro, Toshima, Tokyo 171-8501, Japan
- ⁴¹Saint Petersburg State Polytechnic University, St. Petersburg, Russia
- ⁴²Universidade de São Paulo, Instituto de Física, Caixa Postal 66318, São Paulo CEP05315-970, Brazil
- ⁴³System Electronics Laboratory, Seoul National University, Seoul, Korea
- ⁴⁴Chemistry Department, Stony Brook University, Stony Brook, SUNY, NY 11794-3400, U.S.
- ⁴⁵Department of Physics and Astronomy, Stony Brook University, SUNY, Stony Brook, NY 11794, U.S.
- ⁴⁶SUBATECH (Ecole des Mines de Nantes, CNRS-IN2P3, Université de Nantes) BP 20722 - 44307, Nantes, France
- ⁴⁷University of Tennessee, Knoxville, TN 37996, U.S.
- ⁴⁸Department of Physics, Tokyo Institute of Technology, Oh-okayama, Meguro, Tokyo 152-8551, Japan
- ⁴⁹Institute of Physics, University of Tsukuba, Tsukuba, Ibaraki 305, Japan
- ⁵⁰Vanderbilt University, Nashville, TN 37235, U.S.
- ⁵¹Waseda University, Advanced Research Institute for Science and Engineering, 17 Kikui-cho, Shinjuku-ku, Tokyo 162-0044, Japan
- ⁵²Weizmann Institute, Rehovot 76100, Israel
- ⁵³Yonsei University, IPAP, Seoul 120-749, Korea

We present inclusive charged hadron elliptic flow (v_2) measured over the pseudorapidity range $|\eta| < 0.35$ in Au+Au collisions at $\sqrt{s_{NN}} = 200$ GeV. Results for v_2 are presented over a broad range of transverse momentum ($p_T = 0.2$ –8.0 GeV/c) and centrality (0–60%). In order to study non-flow effects that are not correlated with the reaction plane, as well as the fluctuations of v_2 , we compare two different analysis methods: (1) event plane method from two independent sub-detectors at forward ($|\eta| = 3.1$ –3.9) and beam ($|\eta| > 6.5$) pseudorapidities and (2) two-particle cumulant method extracted using correlations between particles detected at midrapidity. The two event-plane results are consistent within systematic uncertainties over the measured p_T and in centrality 0–40%. There is at most 20% difference of the v_2 between the two event plane methods in peripheral (40–60%) collisions. The comparisons between the two-particle cumulant results and the standard event plane measurements are discussed.

I. INTRODUCTION

Collisions of Au+Au nuclei at the Relativistic Heavy Ion Collider (RHIC) produce matter at very high energy density [1, 2, 3, 4]. The dynamical evolution of this hot and dense medium reflects its state and the degrees of freedom that govern the different stages it undergoes [5, 6, 7]. Azimuthal anisotropy measurements serve as a probe of the degree of thermalization, transport coefficients and the equation of state (EOS) [8, 9, 10] of the produced medium.

Azimuthal correlation measurements in Au+Au collisions at RHIC have been shown to consist of a mixture of jet and harmonic contributions [11, 12, 13, 14]. Jet contributions are found to be relatively small for $p_T \lesssim 2.0$ GeV/c, with away-side jet yields strongly suppressed [13]. Significant modifications to the away-side jet topology have also been reported [15, 16, 17]. The harmonic contributions are typically characterized by the Fourier coefficients,

$$v_n = \langle \cos(n[\phi - \Psi_{\text{RP}}]) \rangle \quad (n = 1, 2, \dots), \quad (1)$$

where ϕ represents the azimuthal emission angle of a charged hadron and Ψ_{RP} is the azimuth of the reaction plane defined as containing both the direction of the impact parameter vector and the beam axis. The brackets denote statistical averaging over particles and events. The first two harmonics v_1 and v_2 are referred to as directed and elliptic flow, respectively.

It has been found that at low p_T ($p_T \lesssim 2.0$ GeV/c) the magnitude and trends of \tilde{v}_2 are under-predicted by hadronic cascade models supplemented with string dynamics [18], but are well reproduced by models which either incorporate hydrodynamic flow [7, 9] with a first order phase transition and rapid thermalization, $\tau \sim 1$ fm/c [19], or use a quasi-particle ansatz but include more than just 2-to-2 interactions [20].

The mass dependence of v_2 as a function of p_T has been studied using identified baryons and mesons [19, 21] and empirical scaling of elliptic flow per constituent quark was observed when the signal and the p_T of the hadron were divided by the number of constituent quarks n_q ($n_q = 2$ for mesons, 3 for baryons). This scaling is most clearly observed by plotting the data as a function of transverse kinetic energy $\text{KE}_T \equiv m_T - m = \sqrt{p_T^2 + m^2} - m$ [22], where m_T and m denote the transverse mass and mass of the particle, respectively. A recent study [23] finds that the constituent quark scaling holds up to $\text{KE}_T \approx 1$ GeV. This indicates partonic, rather than hadronic flow, and suggests that the bulk

matter collectivity develops before hadronization takes place [24, 25, 26]. Results for the v_2 of the ϕ meson further validate the observation of partonic collectivity. The ϕ is not expected to be affected by hadronic interactions in the late stages of the medium evolution, due to its small interaction cross section with non-strange hadrons [27].

All of the v_2 measurements referenced above were performed using the event plane method [28]. In PHENIX the event plane was determined at forward and backward pseudorapidities ($|\eta| = 3.1\text{--}3.9$) with the assumption that correlations induced by elliptic flow dominate over all other non-flow correlations [19]. Non-flow correlations are those which are not correlated with the reaction plane. Common sources of non-flow correlations include jets, the near-side ridge, quantum correlations and resonance decays. Simulation studies [19, 29] have shown that the correlations from jets and dijets become negligible when the rapidity separation between the particles and the event plane is greater than three units. Thus we expect that the event plane at forward pseudorapidities $|\eta| = 3.1\text{--}3.9$ in the PHENIX experiment would not have significant jet-correlation with particles measured within the PHENIX central arm spectrometer covering the pseudorapidity window $|\eta| < 0.35$. PHOBOS has observed that in central Au+Au collisions there is a ridge of particles [30] that are correlated in azimuthal angle with a high- p_T particle and that this ridge of particles extends to $|\eta| < 4$ (for mid-rapidity triggers). The ridge could produce a non-flow correlation that we can provide information by using our v_2 measurements that are made with different techniques and at different rapidities.

Event-by-event flow fluctuations can also affect the magnitude of the extracted flow signal [31]. This occurs because the event plane at forward pseudorapidities is reconstructed using particles from participant nucleons whose positions fluctuate event-by-event. Assuming that v_2 fluctuates according to a Gaussian distribution, the v_2 fluctuation is proportional to the fluctuation of the initial geometry. This effect scales as $1/N_{\text{part}}$, where N_{part} denotes the number of participant nucleons. The difference between v_2 values obtained from different methods can be quantitatively understood in terms of non-flow and fluctuation effects [32].

Hence in this paper we will compare the v_2 results from the event plane determined at two different pseudorapidities with the goal to investigate the sensitivity of v_2 to non-flow and fluctuation effects. Additionally, we extract the elliptic flow with the two-particle cumulant method, which is expected to have higher sensitivity to non-flow contributions to v_2 .

In this paper, we describe the PHENIX measurements of elliptic flow (v_2) at midrapidity ($|\eta| < 0.35$) in Au+Au collisions at $\sqrt{s_{NN}} = 200$ GeV obtained from a cumulant analysis of two-particle azimuthal correlations and the event plane method over a broad range of p_T ($p_T = 0.2\text{--}$

*Deceased

†PHENIX Spokesperson: jacak@skipper.physics.sunysb.edu

8 GeV/ c) and centrality (0–60%). The paper is organized as follows: Section II describes the PHENIX apparatus, with an emphasis on the detectors relevant to the presented results, as well as the track selections used in the analysis. Section III gives details of the event-plane and the cumulant methods as applied in PHENIX. Section IV discusses the systematic uncertainties of the event-plane and cumulant methods. The results from the two methods are reported in Section V. Section VI presents a comparison of v_2 results across different experiments and discussion. The v_2 values obtained from the different methods are tabulated in the Appendix.

II. EXPERIMENTAL ANALYSIS

A. The PHENIX detector

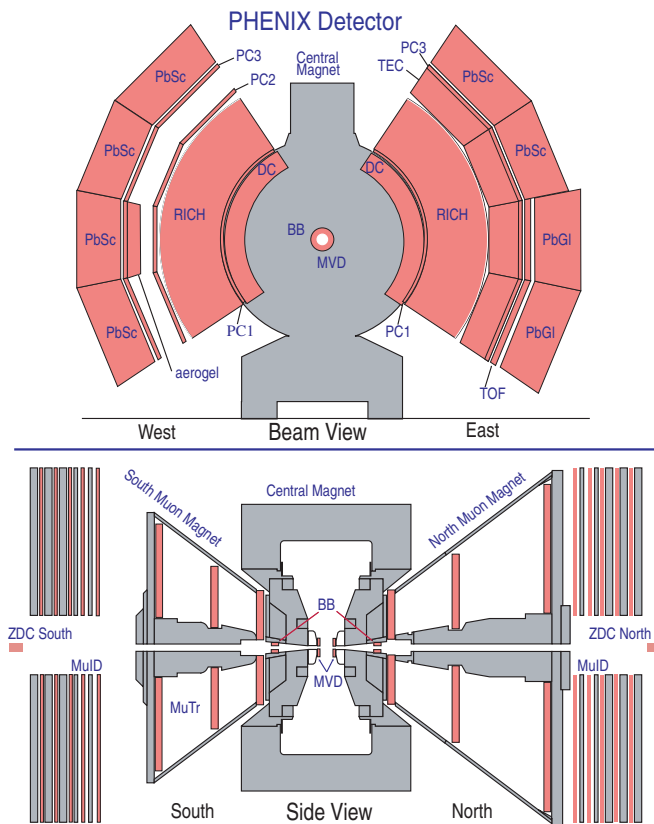


FIG. 1: PHENIX experimental layout in 2004. The top panel shows the PHENIX central arm spectrometers viewed along the beam axis. The bottom panel shows a side view of the PHENIX muon arm spectrometers.

The PHENIX detector consists of two central spectrometer arms at midrapidity that are designated East and West for their location relative to the interaction region, and two muon spectrometers at forward rapidity, similarly called North and South. A detailed description of the PHENIX detector can be found in Ref. [33].

The layout of the PHENIX detector during data taking in 2004 is shown in Fig. 1. Each central spectrometer arm covers a pseudorapidity range of $|\eta| < 0.35$ subtending 90 degrees in azimuth and is designed to detect electrons, photons and charged hadrons. Charged particles are tracked by drift chambers (DC) positioned between 2.0 m and 2.4 m radially outward from the beam axis and layers of multi-wire proportional chambers with pad readout (two in the east arm and three in the west arm) PC1, PC2 and PC3 located at a radial distance of 2.4 m, 4.2 m and 5 m, respectively. Particle identification is provided by Ring Imaging Čerenkov counters (RICH), a time-of-flight scintillator wall (TOF), and two types of electromagnetic calorimeters (EMCAL), the lead scintillator (PbSc) and lead glass (PbGl).

The detectors used to characterize each event are the beam-beam counters (BBCs) [34] and the zero-degree calorimeters (ZDCs) [35]. These detectors are used to determine the time of the collision, the position of the collision vertex along the beam axis and the collision centrality and also provide the event trigger. In this analysis the BBCs are also used to determine the event plane. Each BBC is composed of 64 elements and a single BBC element consists of a one-inch diameter mesh dynode photomultiplier tube (PMT) mounted on a 3 cm long quartz radiator. The BBCs are installed on the north and south sides of the collision point along the beam axis at a distance of 144 cm from the center of the interaction region and surround the beam pipe. The BBC acceptance covers the pseudorapidity range $3.1 < |\eta| < 3.9$ and the full range of azimuthal angles.

The ZDCs are hadronic calorimeters located on both sides of the PHENIX detector. Each ZDC is mechanically subdivided into 3 identical modules of two interaction lengths. They cover a pseudorapidity range of $|\eta| > 6.5$ and measure the energy of the spectator neutrons with a 20 GeV energy resolution [35]. The shower maximum detectors (ZDC-SMDs) are scintillator strip hodoscopes between the first and second ZDC modules. This location approximately corresponds to the maximum of the hadronic shower. The horizontal coordinate is sampled by 7 scintillator strips of 15 mm width, while the vertical coordinate is sampled by 8 strips of 20 mm width. The active area of a ZDC-SMD is 105 mm \times 110 mm (horizontal \times vertical dimension). Scintillation light is delivered to a multichannel PMT M16 by wavelength-shifter fibers. The ZDC-SMD position resolution depends on the energy deposited in the scintillator. It varies from < 3 mm when the number of particles exceeds 100, to 10 mm for a smaller number of particles.

B. Event selection

For the analyses presented here we used approximately 850×10^6 minimum-bias triggered events. The minimum-bias trigger was defined by a coincidence between North and South BBC signals and an energy

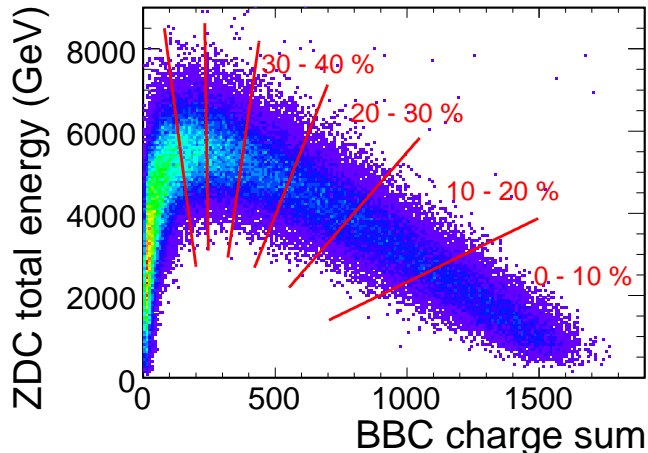


FIG. 2: The correlation between ZDC energy and BBC charge sum for Au + Au collisions at $\sqrt{s_{NN}} = 200$ GeV. Solid lines represent the corresponding centrality boundaries up to 60% centrality bin.

threshold of one neutron in the ZDCs. The events are selected offline to be within a z -vertex of less than 30 cm from the nominal center of the PHENIX spectrometer. This selection corresponds to $92.2^{+2.5}_{-3.0}\%$ of the 6.9 barn Au+Au inelastic cross section at $\sqrt{s_{NN}} = 200$ GeV [36]. The event centrality was determined by correlating the charge detected in the BBCs with the energy measured in the ZDCs, as shown in Fig. 2.

A Glauber model Monte-Carlo simulation [37, 38, 39] that includes the responses of BBC and ZDC gives an estimate of the average number of participating nucleons $\langle N_{\text{part}} \rangle$ for each centrality class. The simulation did not include fluctuations in the positions of the nucleons which give rise to eccentricity fluctuations. Table I lists the calculated values of $\langle N_{\text{part}} \rangle$ for each centrality class.

TABLE I: Centrality classes and average number of participant nucleons $\langle N_{\text{part}} \rangle$ obtained from a Glauber Monte-Carlo simulation of the BBC and ZDC responses for Au+Au collision at $\sqrt{s_{NN}} = 200$ GeV. Each centrality class is expressed as a percentage of $\sigma_{\text{AuAu}} = 6.9$ b inelastic cross section. Errors denote systematic uncertainties from the Glauber MC simulation.

Centrality	$\langle N_{\text{part}} \rangle$
0-10%	325.2 ± 3.3
10-20%	234.6 ± 4.7
20-30%	166.6 ± 5.4
30-40%	114.2 ± 4.4
40-50%	74.4 ± 3.8
50-60%	45.5 ± 3.3

C. Track selection

Charged particle tracks are measured using information from the DC, PC1 and PC3 detectors and the z -vertex from the BBC. The DC has 12 wire planes which are spaced at 0.6 cm intervals along the radial direction from the beam axis. Each wire provides a track position measurement, with better than 150 μm spatial resolution in the azimuthal (ϕ) direction. The PC1 provides a space point in the ϕ and beam directions, albeit with lower resolution. This space point and the vertex position help determine the three-dimensional momentum vector by providing the polar angle for charged tracks at the exit of the DC. Trajectories are confirmed by requiring matching hits at PC3 to reduce secondary background. Tracks are then projected back to the collision vertex through the magnetic field to determine the momentum \vec{p} [40]. The momentum resolution is $\delta p/p \simeq 0.7\% \oplus 1.0\% \times p$ (GeV/c). The momentum scale is known to 0.7%, as determined from the reconstructed proton mass using the TOF detector. Further details on track reconstruction and momentum determination can be found in Refs. [39, 40].

The tracks reconstructed by the DC which do not originate from the event vertex have been investigated as potential background to the charged particle measurement. The main background sources include secondary particles from decays and e^+e^- pairs from the conversion of photons in the material between the vertex and the DC [39]. Tracks are required to have a hit in the PC3, as well as in the EMCAL, within at most 2σ of the expected hit location in both the azimuthal and beam directions. This cut reduces the background not originating in the direction of the vertex. In order to reduce the conversion background we further require tracks to have $E/p_T > 0.2$, where E denotes the energy deposited in the EMCAL and p_T is the transverse momentum of particles measured in the DC. Since most of the electrons from photon conversion are genuine low p_T particles that were reconstructed as high p_T particles, requiring a large deposit of energy in the EMCAL suppresses the electron background [41]. We also require that there are no associated hits in the RICH. The RICH is filled with CO_2 gas at atmospheric pressure and has a charged particle threshold $\gamma_{\text{th}} = 35$ to emit Čerenkov photons.

III. METHODS OF AZIMUTHAL ANISOTROPY MEASUREMENT

In this section we introduce the methods for azimuthal anisotropy measurements as used in the PHENIX experiment. Section III.A describes the event plane method using the BBCs and ZDC-SMDs detectors and Sec. III.B describes the two-particle cumulant method.

A. Event plane method

The event plane method [28] uses the azimuthal anisotropy signal to estimate the angle of the reaction plane. The estimated reaction plane is called the ‘‘event plane’’ and is determined for each harmonic of the Fourier expansion of the azimuthal distribution. The event flow vector $\vec{Q}_n = (Q_x, Q_y)$ and azimuth of the event plane Ψ_n for n -th harmonic of the azimuthal anisotropy can be expressed as

$$Q_x \equiv |\vec{Q}_n| \cos(n\Psi_n) = \sum_i^M w_i \cos(n\phi_i), \quad (2)$$

$$Q_y \equiv |\vec{Q}_n| \sin(n\Psi_n) = \sum_i^M w_i \sin(n\phi_i), \quad (3)$$

$$\Psi_n = \frac{1}{n} \tan^{-1} \left(\frac{Q_y}{Q_x} \right), \quad (4)$$

where M denotes the number of particles used to determine the event plane, ϕ_i is the azimuthal angle of each particle, and w_i is the weight chosen to optimize the event plane resolution. Once the event plane is determined, the elliptic flow v_2 can be extracted by correlating the azimuthal angle of emitted particles ϕ with the event plane

$$v_2 = \frac{v_2^{obs}}{\text{Res}\{\Psi_n\}} = \frac{\langle \cos(2[\phi - \Psi_n]) \rangle}{\langle \cos(2[\Psi_n - \Psi_{RP}]) \rangle}, \quad (5)$$

where ϕ is the azimuthal angle of tracks in the laboratory frame, Ψ_n is the n -th order event plane and the brackets denote an average over all charged tracks and events. The denominator $\text{Res}\{\Psi_n\}$ is the event plane resolution that corrects for the difference between the estimated event plane Ψ_n and true reaction plane Ψ_{RP} .

In this paper the second-harmonic event planes were independently determined with two BBCs located at forward (BBC South, referred to as BBCS) and backward (BBC North, referred to as BBCN) pseudorapidities $|\eta| = 3.1\text{--}3.9$ [19]. The difference between the two independent event planes was used to estimate the event plane resolution. The planes were also combined to determine the event plane for the full event. A large pseudorapidity gap between the charged particles detected in the central arms and the event plane at the BBCs reduces the effect of possible non-flow contributions, especially those from dijets [29]. The measured v_2 of hadrons in the central arms with respect to the combined second-harmonic BBC event plane will be denoted throughout this paper as $v_2\{\text{BBC}\}$.

Two first-harmonic event planes were also determined using spectator neutrons at the two shower maximum detectors (ZDC-SMDs) that are sandwiched between the first and second modules of the ZDCs. Forward (ZDCS) and backward (ZDCN) SMDs which cover pseudorapidity $|\eta| > 6.5$ were used. The measured v_2 of hadrons in the central arms determined with respect to the first-harmonic ZDC-SMD event plane will be denoted as $v_2\{\text{ZDC-SMD}\}$.

The pseudorapidity gap between the hadrons measured in the central arms and the ZDC-SMDs is larger than that for the BBCs which could cause a further reduction of non-flow contributions on $v_2\{\text{ZDC-SMD}\}$. Since the ZDC-SMD measures spectator neutrons, the ZDC-SMD event plane should be insensitive to fluctuations in the participant event plane. Hence fluctuations in $v_2\{\text{ZDC-SMD}\}$ should be suppressed up to fluctuations in the spectator positions.

For completeness, two further event planes are defined 1) a combined event plane defined by the weighted average of event planes at the forward and backward pseudorapidities for both BBCs and ZDC-SMDs, and 2) an event plane found using tracks in the central arm. The event plane at the central arms (CNT) is only used to estimate the resolution of BBC and ZDC-SMD event planes by using three subevents combination of the ZDC-SMD, BBC and CNT.

1. Event plane determination

To determine an event plane the contribution at each azimuthal angle needs to be appropriately weighted depending on the detector used. For the BBC we chose the weights to be the number of particles detected in each phototube, while for the ZDC-SMD the weights were based on the energy deposited in each of the SMD strips. For the CNT event plane the weight was taken to be proportional to p_T up to 2 GeV/ c and constant for $p_T > 2$ GeV/ c . For the CNT event plane we also adopted a unit weight ($w_i = 1$) and found that the resulting CNT event plane resolution extracted by comparing the CNT event plane with the BBC and ZDC-SMD planes was nearly identical when using the p_T -dependent or unit weights.

Corrections were performed to remove possible biases from the finite acceptance of the BBC and ZDC-SMD. In this analysis, we applied two corrections called the re-centering and shift methods. In the re-centering method, event flow vectors are shifted and normalized to a Gaussian distribution by using the mean $\langle Q \rangle$ and width σ of flow vectors;

$$Q'_x = \frac{Q_x - \langle Q_x \rangle}{\sigma_x}, \quad Q'_y = \frac{Q_y - \langle Q_y \rangle}{\sigma_y}. \quad (6)$$

This correction reduces the dependence of the event plane resolution on the laboratory angle. Most acceptance effects were removed by the application of the re-centering method. However, remaining small corrections were applied after re-centering using the shift method [28], in which the reaction plane is shifted by $\Delta\Psi_n$ defined by

$$n\Delta\Psi_n(\Psi_n) = \sum_{k=1}^{k_{\max}} \frac{2}{k} [-\langle \sin(kn\Psi_n) \rangle \cos(kn\Psi_n) + \langle \cos(kn\Psi_n) \rangle \sin(kn\Psi_n)], \quad (7)$$

where $k_{\max} = 8$ in this analysis. The shift ensures that $dN/d\Psi_n$ is isotropic. When k_{\max} was reduced to

$k_{\max} = 4$, the difference in the extracted v_2 was negligible and thus we include no systematic uncertainty due to the choice of k_{\max} in our v_2 results.

Independent corrections were applied to each centrality selection in 5% increments and in 20 cm steps in z -vertex in order to optimize the event plane resolution. The corrections were also done for each experimental run (the duration of a run is typically 1-3 hours) to minimize the possible time-dependent response of detectors.

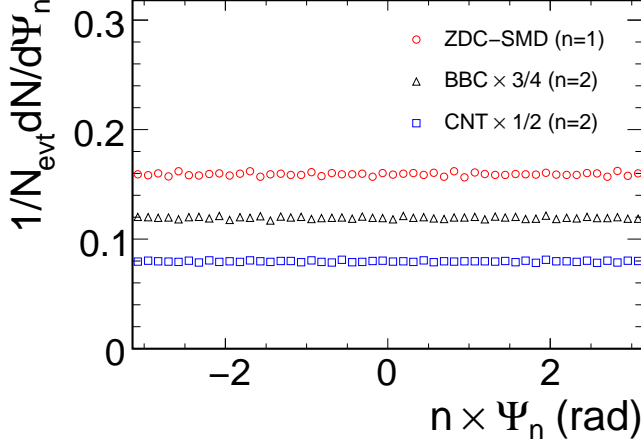


FIG. 3: Event plane distributions after applying all corrections for the ZDC-SMD (circles), BBC (triangles) and CNT (squares). The statistical error bars are smaller than the symbols. The distributions for the BBC and CNT event planes are scaled by 3/4 and 1/2 to improve visibility.

Figure 3 shows event plane distributions for a subsample of the entire data set. After all corrections are applied the event plane distributions are isotropic.

2. Event plane resolution

The event plane resolution for v_2 was evaluated by both the two-subevents and three-subevents methods. In the two-subevents method the event plane resolution [28] is expressed as

$$\langle \cos(kn[\Psi_n - \Psi_{\text{RP}}]) \rangle = \frac{\sqrt{\pi}}{2\sqrt{2}} \chi_n e^{-\chi_n^2/4} \times \left[I_{(k-1)/2} \left(\frac{\chi_n^2}{4} \right) + I_{(k+1)/2} \left(\frac{\chi_n^2}{4} \right) \right], \quad (8)$$

where $\chi_n = v_n \sqrt{2M}$, M is the number of particles used to determine the event plane Ψ_n , I_k is the modified Bessel function of the first kind and $k = 1$ for the second harmonic BBC event plane. For the ZDC-SMD event plane the resolution is estimated with both $k = 1$ or 2 in Eq. (8). We will discuss the difference between these estimates in Sec. IV A.

To determine the event plane resolution we need to determine χ_n . Since the North and South BBCs have

approximately the same η coverage, the event plane resolution of each sub-detector is expected to be the same. The same is true for the North and South ZDC-SMDs. Thus, the subevent resolution for South and North event planes can be expressed as

$$\langle \cos(2[\Psi_n^{\text{S(N)}} - \Psi_{\text{RP}}]) \rangle = \sqrt{\langle \cos(2[\Psi_n^{\text{S}} - \Psi_n^{\text{N}}]) \rangle}, \quad (9)$$

where $\Psi_n^{\text{S(N)}}$ denotes the event plane determined by the South (North) BBC or ZDC-SMD. Once the subevent resolution is obtained from Eq. (9), one can calculate χ_n^{sub} using Eq. (8). The χ_n for the full event can then be estimated by $\chi_n = \sqrt{2} \chi_n^{\text{sub}}$. This is then substituted into Eq. (8) to give the full event resolution. Since the multiplicity of the full event is twice as large as that of the subevent, χ_n is proportional to \sqrt{M} .

In the three-subevents method the resolution of each subevent is calculated by adding a reference event plane Ψ_n^{C} in Eq. (9):

$$\text{Res}\{\Psi_l^{\text{A}}\} = \sqrt{\langle \cos(2[\Psi_l^{\text{A}} - \Psi_m^{\text{B}}]) \rangle} \times \sqrt{\frac{\langle \cos(2[\Psi_n^{\text{C}} - \Psi_l^{\text{A}}]) \rangle}{\langle \cos(2[\Psi_m^{\text{B}} - \Psi_n^{\text{C}}]) \rangle}}, \quad (10)$$

where l, m, n are the harmonics of the event plane for subevent A, B and C, respectively. The multiplicity of each subevent is not necessarily the same in Eq. (10).

The resolution of each sub-detector for the BBC and ZDC-SMD can be evaluated with the three-subevents method. For the BBC event plane the reference event plane is chosen to be the ZDC-SMD event plane and vice versa. We found that the agreement of the event plane resolutions for BBCS and BBCN is much better than 1%, while the ZDCS and ZDCN resolutions are comparable with each other within 2%.

Figure 4 shows the full-event resolution as a function of centrality. The resolution of ZDC-SMD is much smaller than that of BBC because the resolution of the first-harmonic event plane is proportional to $(\chi_1)^2$. The dashed lines are the resolutions obtained from the three-subevents method with the CNT event plane as the reference plane. For example, the BBC event plane resolution is estimated by substituting $\Psi_l^{\text{A}} \rightarrow \Psi_2^{\text{BBC}}$, $\Psi_m^{\text{B}} \rightarrow \Psi_2^{\text{CNT}}$, and $\Psi_n^{\text{C}} \rightarrow \Psi_1^{\text{ZDC-SMD}}$ in Eq. (10). By including the CNT event plane, the BBC resolution increases by about 3% compared to that of the two-subevents method. For the ZDC-SMD we observe the opposite effect, namely the resolution decreases by about 8%. In Sec. VI the resulting $v_2\{\text{BBC}\}$ and $v_2\{\text{ZDC-SMD}\}$, corrected by the resolution obtained using the ZDC-BBC-CNT combination, will be compared to those with the resolution determined from South-North subevents. Table II summarizes the event plane resolutions.

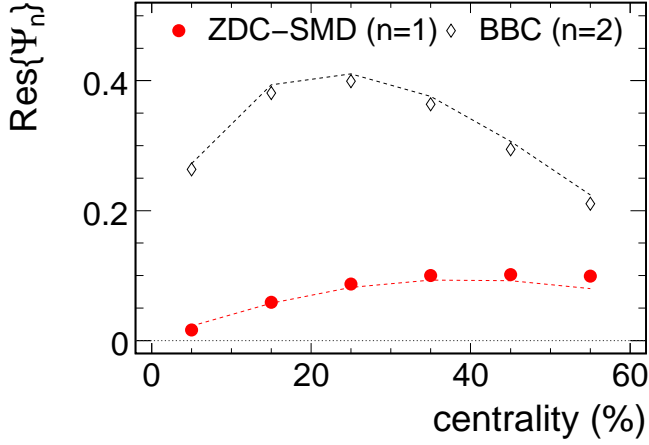


FIG. 4: Full-event resolutions for the ZDC-SMD (filled circles) and BBC (open diamonds) from the two-subevents method, Eq. (8), as a function of centrality in Au+Au at $\sqrt{s_{NN}} = 200$ GeV. The dashed lines represent resolutions from the three-subevents method with the CNT event plane as a reference. Statistical errors are smaller than the symbols.

TABLE II: Event plane resolutions for centrality 0–60% at $\sqrt{s_{NN}} = 200$ GeV. S-N denotes the resolutions estimated from South and North correlation of BBC and ZDC-SMD using Eq. (8) and (9), and resolutions for ZDC-BBC-CNT are estimated from Eq. (10). The errors are statistical only.

Centrality	$\text{Res}\{\Psi_2^{\text{BBC}}\}$	
	S-N	ZDC-BBC-CNT
0–10%	0.2637 ± 0.0003	0.272 ± 0.003
10–20%	0.3809 ± 0.0002	0.394 ± 0.001
20–30%	0.3990 ± 0.0002	0.4106 ± 0.0008
30–40%	0.3634 ± 0.0002	0.3759 ± 0.0007
40–50%	0.2943 ± 0.0003	0.3067 ± 0.0007
50–60%	0.2106 ± 0.0004	0.2240 ± 0.0009

Centrality	$\text{Res}\{\Psi_1^{\text{ZDC-SMD}}\}$	
	S-N	ZDC-BBC-CNT
0–10%	0.02 ± 0.01	0.0223 ± 0.0003
10–20%	0.059 ± 0.003	0.0574 ± 0.0002
20–30%	0.087 ± 0.002	0.0818 ± 0.0002
30–40%	0.100 ± 0.002	0.0928 ± 0.0002
40–50%	0.102 ± 0.002	0.0920 ± 0.0002
50–60%	0.100 ± 0.002	0.0798 ± 0.0003

3. Correlation of event planes

Figure 5 shows the correlation of two different event planes as a function of centrality. The first harmonic event plane correlation for South-North detector combinations is negative both for the ZDC-SMDs and the BBCs over all centrality bins, as shown in Fig. 5(a). This is due to the fact that v_1 is an odd function of η . The magnitude of the ZDC-SMDs correlation is about a factor of two larger than that of the BBCs for midcentral collisions. This indicates that the magnitude of v_1

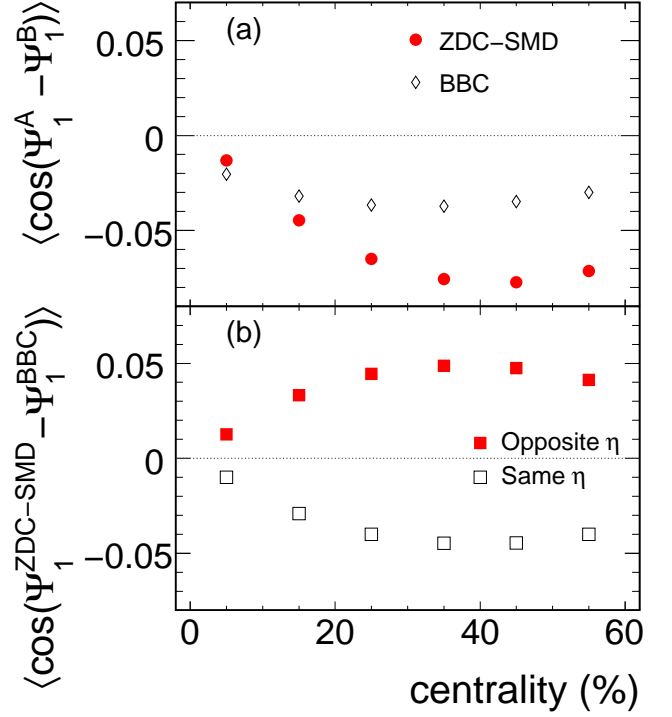


FIG. 5: (a) Correlation of first harmonic event planes between forward and backward ZDC-SMDs (filled circles) and BBCs (open diamonds) as a function of centrality. (b) Correlation of first harmonic event planes between ZDC-SMDs and BBCs as a function of centrality, where filled (open) squares are the correlation for opposite side (same side) of η subevents. Statistical errors are smaller than the symbols.

and/or the subevent multiplicity at higher pseudorapidities are larger compared to that at the BBC location, since the magnitude of the correlation is proportional to $v_1^2 M$. Fig. 5(b) shows the correlation of the first harmonic event planes between BBC and ZDC-SMD. The same-side η correlation is negative while the opposite-side η correlation is positive, which shows that the particles detected at the BBCs (dominantly charged pions emitted from participant nucleons) have the opposite sign of v_1 compared to the spectator neutrons detected at the ZDCs-SMDs.

The correlation of the mixed harmonic event planes provides the sign of v_2 since the correlation is given by the expression [28]

$$\begin{aligned}
& \langle \cos(2[\Psi_1^{\text{ZDC-SMD}} - \Psi_2^{\text{BBC}}]) \rangle \\
& \approx \frac{2}{\pi} (\text{Res}\{\Psi_1^{\text{ZDC-SMD}}\})^2 \text{Res}\{\Psi_2^{\text{BBC}}\} \\
& = \pm 2\sqrt{2} \frac{2}{\pi} \langle \cos(\Psi_1^{\text{ZDCS}} - \Psi_1^{\text{ZDCN}}) \rangle \\
& \quad \times \sqrt{\langle \cos(2[\Psi_2^{\text{BBCS}} - \Psi_2^{\text{BBCN}}]) \rangle}. \quad (11)
\end{aligned}$$

Three assumptions were made to obtain Eq. (11): (1) the BBC and ZDC-SMD are statistically independent, (2) the weak flow limit is applicable, and (3) the subevent

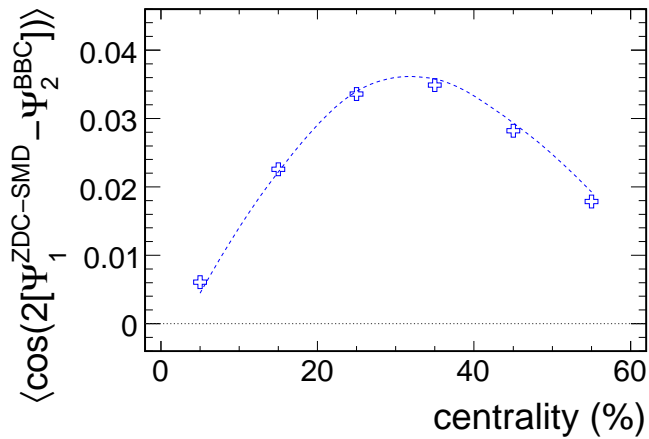


FIG. 6: The correlation between the first harmonic ZDC-SMD and the second harmonic BBC event planes as a function of centrality. The dashed line shows the result obtained using Eq. (11). Statistical errors are smaller than the data symbols.

multiplicity M is equal in the North-South direction for the same detector type. Thus the sign of the correlation of the mixed harmonic event planes in Eq. (11) is determined by the term $\text{Res}\{\Psi_2^{\text{BBC}}\}$, which in turn determines the sign of v_2 measured at the BBC.

Figure 6 shows the mixed harmonic correlation of the ZDC-SMD and BBC event planes as a function of centrality. The approximations in Eq. (11) provide a good description of the magnitude of the measured correlation as shown by the dashed line. The correlation is positive over all centrality bins. This result indicates that the sign of v_2 at the BBC is positive.

B. Cumulant method

In this section, we present the application of the cumulant method for azimuthal anisotropy measurements in PHENIX. This method uses cumulants of multiparticle correlations [42, 43] to extract the azimuthal anisotropy. The cumulant method has been successfully applied in several heavy-ion experiments utilizing detectors with full azimuthal coverage (NA49, STAR) [44, 45]. Here, we describe the first application of the method for a detector with only partial azimuthal coverage. The cumulant method does not require the measurement of the reaction plane, instead the cumulants of multi-particle azimuthal correlations are related to the flow harmonics v_n , where n is the harmonic being evaluated. The cumulants can be constructed in increasing order according to the number of particles that are correlated with each other. Since PHENIX has partial azimuthal coverage, reliable extraction of azimuthal anisotropy requires the choice of a fixed number of particles from each event in order to avoid additional numerical errors [42].

Particles in an event are selected over a fixed p_T range

where there is sufficient multiplicity. These particles (called “integral particles” hereafter) are used to determine integrated flow, that is flow measured over a large (p_T, η) bin. For differential flow measurement, we select particles (called “differential” particles) over small (p_T, η) bins, from which the integral particles are excluded so as to avoid autocorrelations. For each event a fixed number M of particles, chosen at random among the integral particles in the event, are used to reconstruct the integrated flow through the generating function $G_2(z)$ defined by:

$$G_2(z) = \prod_{j=1}^M \left[1 + \frac{w_j}{M} (z^* e^{2i\phi_j} + z e^{-2i\phi_j}) \right], \quad (12)$$

where w_j is the weight, chosen to be equal to 1 in our analysis, ϕ_j is the azimuth of the detected particles, and M is the multiplicity chosen for the integrated flow reconstruction. $G_2(z)$ is a function of the complex variable z . The average of $G_2(z)$ over events is then expanded in a power series to generate multi-particle azimuthal correlations. The generating function of the cumulants, defined by

$$\mathcal{C}_n(z) \equiv M \left(\langle G_n(z) \rangle^{1/M} - 1 \right). \quad (13)$$

generates cumulants of azimuthal correlations to all orders, the lowest being the second order, as detailed in Section II.B of Ref. [42]. The formulas used to compute the cumulants from which the v_2 is computed are given in Appendix B of Ref. [42]. In the case of a perfect acceptance the relations between the anisotropy parameter v_2 and the lowest order cumulants are

$$v_2\{2\}^2 = c_2\{2\}, \quad (14)$$

$$v_2\{4\}^4 = -c_2\{4\}, \quad (15)$$

for the integrated anisotropy. Here $v_2\{2\}$ and $v_2\{4\}$ are the second and fourth order v_2 , respectively; whereas, $c_2\{2\}$ and $c_2\{4\}$ are the second and fourth order cumulants. Because the typical multiplicity of charged hadrons in PHENIX did not allow a reliable calculation of $v_2\{4\}$, we report here only the $v_2\{2\}$ results.

The remaining differential particles in the same event are selected in different (p_T, η) bins and the differential cumulants are calculated from the generating function

$$\mathcal{D}_{2/2}(z) \equiv \frac{\langle e^{2i\psi} G_2(z) \rangle}{\langle G_2(z) \rangle}, \quad (16)$$

where $\langle G(z) \rangle$ denotes an average over all events, and ψ is the azimuth of each differential particle. $\mathcal{D}_{2/2}$ denotes the second order differential cumulant computed with respect to the second order integral cumulant.

The differential $v_{2/2}\{2\}(p_T, \eta)$, the second order differential $\hat{2}$ with respect to the second order integrated $\hat{2}$, is calculated from the relation

$$v_{2/2}\{2\}(p_T, \eta) = \frac{d_{2/2}\{2\}(p_T, \eta)}{v_2\{2\}}, \quad (17)$$

where $d_{2/2}\{2\}(p_T, \eta)$ is the second order differential cumulant. These relations have to be modified through acceptance corrections which are detailed below.

1. Acceptance/efficiency corrections

The central arms detectors in PHENIX have only partial azimuthal coverage and the implementation of the cumulant method requires an additional acceptance correction. In order to correct for the influence of the detector acceptance on the raw anisotropy values, we apply a correction factor using the prescription described in Ref. [42]. The acceptance and efficiency of the detector is characterized by a function $A(\phi, p_T, \eta)$ which is expressed in terms of the Fourier series

$$A(\phi, p_T, \eta) = \sum_{p=-\infty}^{+\infty} a_p(p_T, \eta) e^{ip\phi}. \quad (18)$$

The Fourier coefficients $a_p(p_T, \eta)$ for the detector acceptance were extracted from the fit of the respective azimuthal distributions of integral and differential particles. The coefficients resulting from such fits were then used to calculate the correction factor for the raw values of the v_2 following the procedure detailed in Appendix C of Ref. [42].

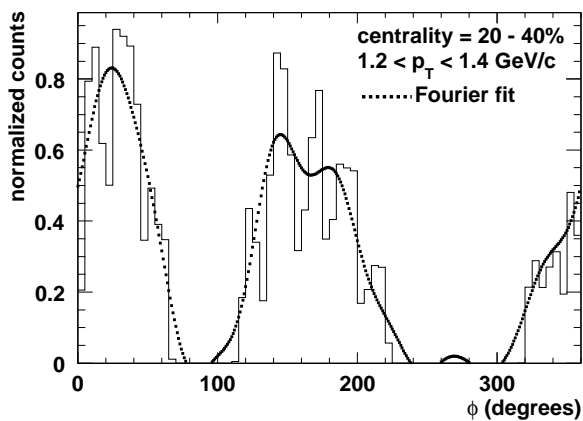


FIG. 7: Azimuthal angular distribution and corresponding Fourier fit for centrality 20–40% and $p_T = 1.2\text{--}1.4$ GeV/ c .

Figure 7 shows a typical azimuthal angular distribution of differential particles detected in the PHENIX central arms and the corresponding Fourier fit used to correct for acceptance inhomogeneities. The Fourier fit reproduces well the overall features of the acceptance profile. This produces typical correction factors that are in the range 1.1–1.2 for the differential flow and depend very little on centrality and p_T , as shown in Fig. 8.

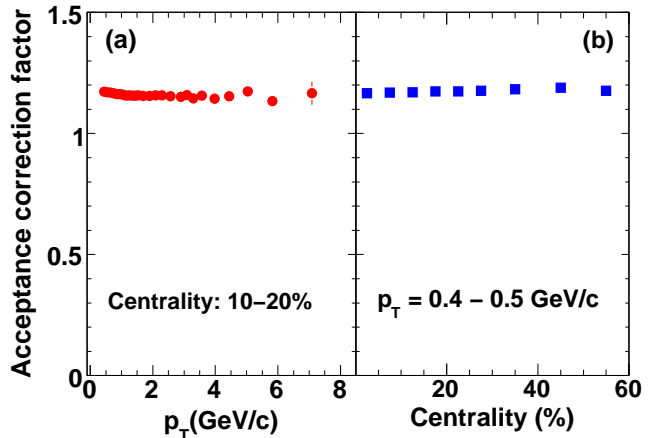


FIG. 8: (a) Acceptance correction factor for differential $v_2\{2\}$ as a function of p_T for centrality 10–20% (b) Acceptance correction factor as a function of centrality for p_T range 0.4–0.5 GeV/ c in Au+Au collisions at $\sqrt{s_{NN}} = 200$ GeV.

2. Simulations

While Fig. 7 shows that the uneven detector acceptance is reproduced by the Fourier fit, a better test of the cumulant method is to use Monte-Carlo simulations, as was done in Ref. [42]. For these tests events were generated with particles having a distribution of the form $1 + 2v_1 \cos \phi + 2v_2 \cos 2\phi$, with known integrated and differential azimuthal anisotropies. The anisotropy was introduced into the events by way of a Fourier weighted selection of the azimuthal angles followed by a random event rotation designed to simulate the random orientation of the reaction plane. The multiplicity of these events was chosen to reflect the typical multiplicity measured with the PHENIX detector and the ϕ angles were chosen from a filter that is representative of the PHENIX acceptance. We extracted Fourier components from these simulated results and applied these to extract corrected elliptic flow values.

Figure 9 shows selected results from these simulations. Corrected differential anisotropy values are compared for various input differential v_2 values, with the integral v_2 kept fixed. The dotted line shows the trend expected if the extracted v_2 is identical to the input value used to generate the events. The good agreement between the input and extracted v_2 attests to the reliability of the analysis method within the acceptance of the PHENIX central arms.

IV. SYSTEMATIC UNCERTAINTIES

In this section, we present the systematic uncertainties on the v_2 from the event plane method (Sec. IV A) and the two-particle cumulant method (Sec. IV B). Table III lists the different sources of systematic errors for each

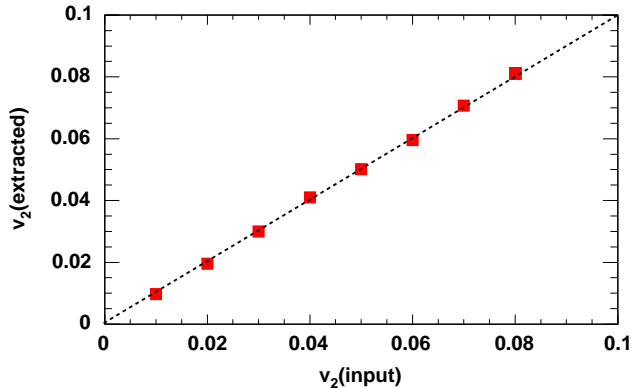


FIG. 9: Comparison of input and extracted differential v_2 values for a fixed integral v_2 of 8%. The dotted line indicates the expectation if input and reconstructed values are the same.

method. The errors in Tab. III are categorized by type:

- A point-to-point error uncorrelated between p_T bins,
- B p_T correlated, all points move in the same direction but not by the same factor,
- C an overall normalization error in which all points move by the same factor independent of p_T .

TABLE III: List of systematic uncertainties given in percent on the $v_2\{\text{ZDC-SMD}\}$, $v_2\{\text{BBC}\}$ and $v_2\{2\}$ measurements. The ranges correspond to different systematic errors for different centrality bins.

Error source	Percentage error		Type
	$v_2\{\text{BBC}\}$	$v_2\{\text{ZDC-SMD}\}$	
Background contribution	< 5% in $p_T < 4$ GeV/c		B
	5–30% in $p_T > 4$ GeV/c		B
Event plane calibration		1–5%	C
Event plane determination	1–4%	1–16%	C
Acceptance effect on event planes	1%	1–25%	C
		$v_2\{2\}$	
Fixed multiplicity		5%	B
Integrated p_T range		3–8%	B
Background correction		6–10%	B

A. Event plane method

1. Background contributions

In order to study the influence of background on our results, we varied one of the track selections while keeping other cuts fixed and investigated the effect on v_2 in the following two cases: (i) the PC3 and EMCAL matching cuts, ± 1.5 and $\pm 2.5\sigma$ matching cuts and (ii) $E > 0.15p_T$

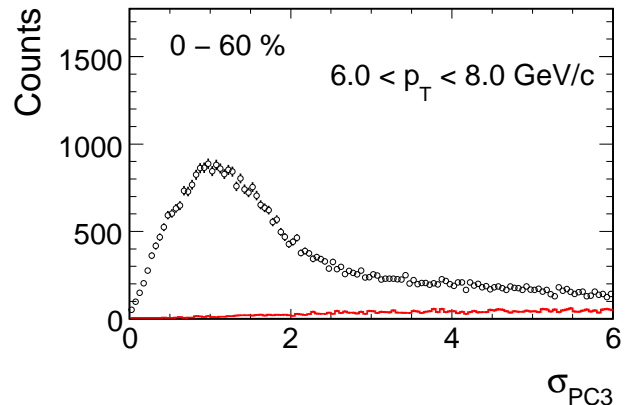


FIG. 10: The radial PC3 matching distribution for real (open circles) and random tracks (solid lines) for $6 < p_T < 8$ GeV/c in centrality 0–60%.

and $E > 0.25p_T$. For both conditions, we found that the difference of the v_2 is 1–2% for $p_T < 4$ GeV/c, and 5–20% for $p_T > 4$ GeV/c depending on p_T and centrality.

The effect of the RICH veto cut has also been studied. Since the contribution of charged π increases without the RICH veto cut, the p/π ratio decreases at high p_T . Thus, the v_2 for charged hadrons could be modified due to the difference of v_2 between protons and π in the range $4 < p_T < 8$ GeV/c. We found that v_2 is 10–20% different without the RICH veto cut for $p_T > 4$ –5 GeV/c, where the charged π starts firing the RICH.

One of the remaining sources of background contribution comes from the random tracks that are accidentally associated with the tracks in PC3. These random tracks have been estimated by swapping the z-coordinate of the PC3 hits and then by associating those hits with the real tracks. Figure 10 shows the comparison of the radial PC3 matching distribution between the real and random tracks for $6 < p_T < 8$ GeV/c. The signal to background ratio S/B is evaluated in the $\sigma_{\text{PC3}} < 2$ window, and is ~ 52 for $6 < p_T < 8$ GeV/c in centrality 0–60%.

The ratio of real and random tracks with and without the $E/p_T > 0.2$ cut is shown as a function of p_T for centrality 0–60% in Fig. 11. The $E/p_T > 0.2$ cut reduces the random tracks and improves the S/B ratio by a factor of ≈ 10 –24 for $p_T > 4$ GeV/c. Since random tracks are not expected to be correlated with the event plane, we assume that their $v_2 = 0$ and evaluate the systematic uncertainty on v_2 to be less than 2% for $p_T > 4$ GeV/c, increasing to 5% for $p_T < 0.5$ GeV/c.

There is a finite residual background contribution even after the $E/p_T > 0.2$ has been applied, as observed in Fig. 10. The residual backgrounds have been estimated by fitting the σ_{PC3} with a double Gaussian while requiring that the signal and residual background σ_{PC3} distribution have the same mean. For the highest p_T bin, we found that the signal to background ratio is ~ 5 for $\sigma_{\text{PC3}} < 2$. The systematic error on v_2 is evaluated by

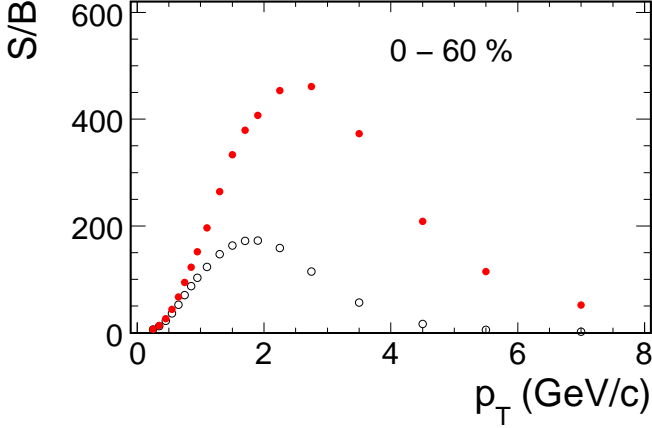


FIG. 11: The ratio of real S to random tracks B as a function of p_T in centrality 0–60%. Solid and open circles show the S/B ratio with and without $E/p_T > 0.2$, respectively.

comparing the measured v_2 with that of signal

$$v_2^S = \left(1 + \frac{B}{S}\right) v_2 - \frac{B}{S} v_2^B, \quad (19)$$

where v_2^S , v_2^B and v_2 are respectively v_2 of signal, background estimated for $\sigma_{PC3} > 3$, and measured within the 2σ matching window. The systematic uncertainties are less than 5% for $p_T < 4$ GeV/ c , and ~ 5 –10% for higher p_T . All the above systematic errors are added in quadrature and the overall systematic error from the background contribution is estimated to vary from $< 5\%$ for $p_T < 4$ GeV/ c to $\sim 30\%$ for higher p_T .

2. Event plane calibrations

The procedures used in the determination and calibration of event planes are the dominant sources of systematic errors on v_2 and are discussed in the following sections.

Different calibration procedures of the BBC event plane were extensively studied for previous Au + Au data sets [19]. We followed the same procedure to study the systematic errors on the BBC and ZDC-SMD event planes. Systematic uncertainties from the shift methods on $v_2\{\text{BBC}\}$ are ~ 1 –5% depending on the centrality. The systematic errors on the $v_2\{\text{ZDC-SMD}\}$ are 1–2% larger than those on $v_2\{\text{BBC}\}$ for centrality 10–30% and 50–60%, although those are still less than 5%.

3. Event plane determination

Figure 12 shows the comparison of $\langle v_2 \rangle$ for different sub-detectors with respect to the BBC and ZDC-SMD event planes as a function of centrality. Systematic errors

are estimated by taking the maximum difference of the v_2 from the South and North event planes to that from the combined South-North event plane scaled by $2/\sqrt{12}$ for each centrality. Systematic errors range from 1–4% for the BBC, and 1–16% for the ZDC-SMD event planes depending on the centrality bins.

4. Effect of non-uniform acceptance on v_2

In this subsection we discuss the effect of non-uniform acceptance on the measured v_2 . In practice, the imperfect azimuthal acceptance of the BBC or ZDC-SMD or the central arms could induce an azimuthal-dependent event plane resolution and/or smear the magnitude of v_2 . In order to study the possible effect of non-uniform acceptance, the measured v_2 is decomposed into X and

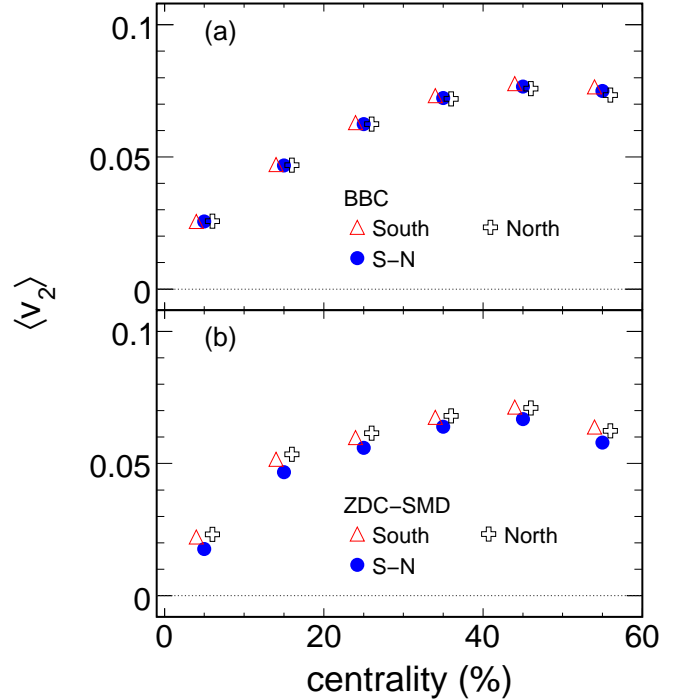


FIG. 12: (a) Comparison of $\langle v_2 \rangle$ averaged over $0.2 < p_T < 8$ GeV/ c as a function of centrality for the BBC event planes. Open triangles and crosses represent the v_2 with respect to the event planes from South and North sub-detectors and filled circles show the v_2 from combined South-North event planes. Results from South and North event planes are shifted in the x-direction to improve visibility. (b) The same comparison for the ZDC-SMD event planes. Only statistical errors are shown and they are smaller than the symbols.

Y components [46]:

$$\begin{aligned} v_2^X &= \frac{\sqrt{2} \langle \cos(2\phi) \cos(2\Psi_n^A) \rangle}{a_4^+ \text{Res}\{\Psi_n^A; X\}}, \\ v_2^Y &= \frac{\sqrt{2} \langle \sin(2\phi) \sin(2\Psi_n^A) \rangle}{a_4^- \text{Res}\{\Psi_n^A; Y\}}, \end{aligned} \quad (20)$$

where ϕ denotes the azimuthal angle of hadrons measured in the central arms and $a_4^\pm = 1 \pm \langle \cos(4\phi) \rangle$ are the acceptance correction factors of the measured v_2 in the central arms. The coefficient a_4^\pm should be unity in the case of perfect azimuthal acceptance. $\text{Res}\{\Psi_n^A; X\}$ and $\text{Res}\{\Psi_n^A; Y\}$ denote the event plane resolution for v_2^X and v_2^Y respectively and are expressed as

$$\begin{aligned} \text{Res}\{\Psi_l^A; X\} &= \sqrt{\langle \cos(2\Psi_l^A) \cos(2\Psi_m^B) \rangle} \\ &\times \sqrt{\frac{\langle \cos(2\Psi_n^C) \cos(2\Psi_l^A) \rangle}{\langle \cos(2\Psi_m^B) \cos(2\Psi_n^C) \rangle}}, \\ \text{Res}\{\Psi_l^A; Y\} &= \sqrt{\langle \sin(2\Psi_l^A) \sin(2\Psi_m^B) \rangle} \\ &\times \sqrt{\frac{\langle \sin(2\Psi_n^C) \sin(2\Psi_l^A) \rangle}{\langle \sin(2\Psi_m^B) \sin(2\Psi_n^C) \rangle}}, \end{aligned} \quad (21)$$

where l, m, n are the harmonics of event planes for subevents A, B, and C, respectively. Another acceptance effect from the difference between $\text{Res}\{\Psi_n^A; X\}$ and $\text{Res}\{\Psi_n^A; Y\}$ is discussed below.

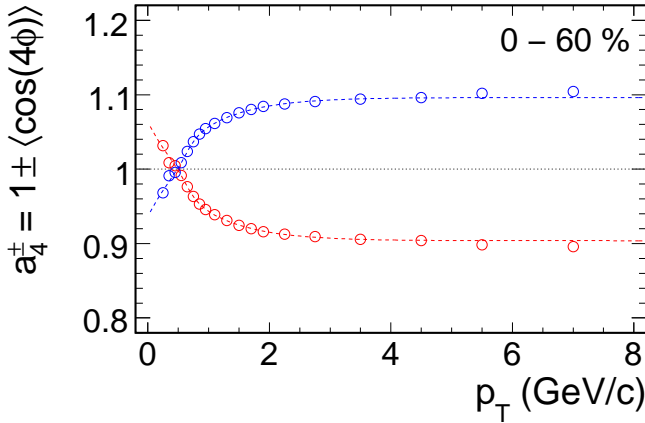


FIG. 13: Acceptance correction factors a_4^\pm in the central arms as a function of p_T for centrality 0–60%. Correction factors become unity for a perfect azimuthal acceptance. Statistical errors are smaller than the symbols.

Figure 13 shows the acceptance correction factor a_4^\pm as a function of p_T in the central arms for centrality 0–60%. The p_T dependence is parameterized by

$$a_4^\pm(p_T) = 1 \mp \left(p_0 e^{-p_1 p_T} + \frac{p_2}{1 + e^{(p_T - p_3)/p_4}} + p_5 \right), \quad (22)$$

where p_n ($n = 0, 1, \dots, 5$) are free parameters. From the fit, we get $p_0 = 0.131$, $p_1 = 1.203$, $p_2 = 0.029$, $p_3 = 0.640$, $p_4 = 0.096$ and $p_5 = -0.097$. There is no centrality dependence of the acceptance corrections in the measured centrality range and these same correction factors are applied for all centrality bins.

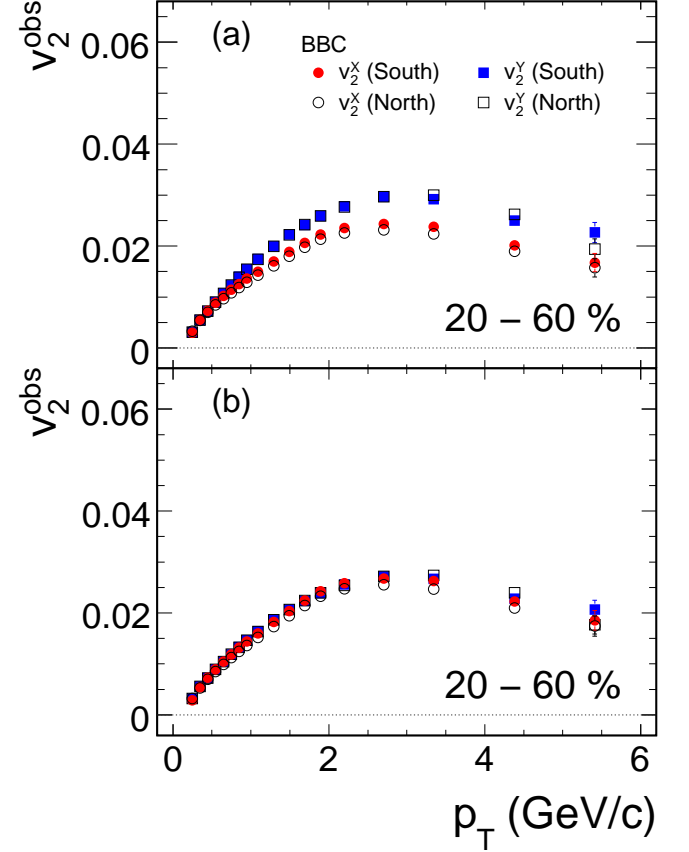


FIG. 14: (a) Raw $v_2\{\text{BBC}\}$ without the acceptance correction as a function of p_T in centrality 20–60% for v_2^X (filled circles), v_2^Y (filled squares) with the South BBC event plane and or v_2^X (open circles), v_2^Y (open squares) with the North BBC event plane. (b) The same comparison with the acceptance correction.

Figure 14 shows the raw $v_2\{\text{BBC}\}$ as a function of p_T in 20–60% centrality bin. v_2^Y is systematically higher than v_2^X for $p_T > 1$ GeV/c as shown in Fig. 14(a). Figure 14(b) shows that v_2^X and v_2^Y agree with each other after dividing v_2^{obs} by a_4^\pm , the remaining difference between them being accounted for as a systematic error. For the ZDC-SMD event plane we observed a similar trend for v_2^X and v_2^Y .

A possible non-uniform acceptance of the BBC and ZDC-SMD could lead to the difference between $\text{Res}\{\Psi_n; X\}$ and $\text{Res}\{\Psi_n; Y\}$. If the azimuthal coverage of both detectors is perfect, $\text{Res}\{\Psi_n; X\}$ and $\text{Res}\{\Psi_n; Y\}$ should be identical. Therefore, the effect of the acceptance of the detector on the event plane resolution can

be assessed by comparing $\text{Res}\{\Psi_n; X\}$ and $\text{Res}\{\Psi_n; Y\}$.

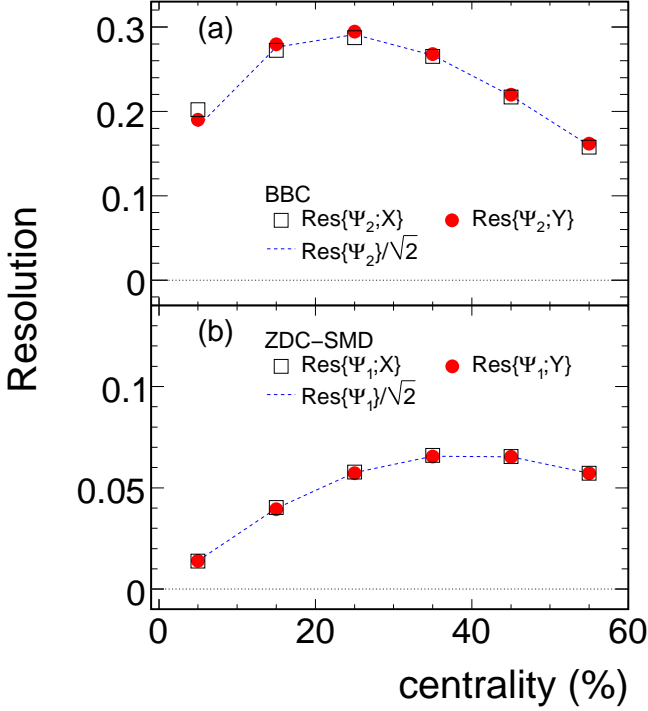


FIG. 15: (a) Comparison of $\text{Res}\{\Psi_n; X\}$ (open squares) and $\text{Res}\{\Psi_n; Y\}$ (filled circles) with $\text{Res}\{\Psi_n\}$ (dashed lines) for the BBC event plane ($n = 2$) as a function of centrality. The resolutions are calculated by using Eq. (21) with the ZDC-SMD, BBC and CNT event planes. $\text{Res}\{\Psi_n\}$ is divided by $\sqrt{2}$ in order to compare $\text{Res}\{\Psi_n; X\}$ and $\text{Res}\{\Psi_n; Y\}$. (b) The same comparison for the ZDC-SMD event plane ($n = 1$). Only statistical errors are shown and are smaller than symbols.

Figure 15 shows $\text{Res}\{\Psi_n; X\}$ and $\text{Res}\{\Psi_n; Y\}$ of the BBC and ZDC-SMD as a function of centrality. The resolutions are calculated by using Eq. (21) with the ZDC-SMD, BBC and CNT event planes. $\text{Res}\{\Psi_n; X\}$ was comparable with $\text{Res}\{\Psi_n; Y\}$ for both the BBC and ZDC-SMD event planes. They also agreed, within statistical errors, with the expected resolution, namely the full event resolution scaled by $1/\sqrt{2}$. We also evaluated $\text{Res}\{\Psi_n; X\}$ and $\text{Res}\{\Psi_n; Y\}$ of BBC and ZDC-SMD for the two-subevents method. $\text{Res}\{\Psi_2^{\text{BBC}}; X\}$ was consistent with $\text{Res}\{\Psi_2^{\text{BBC}}; Y\}$. However, for the ZDC-SMD event plane, $\text{Res}\{\Psi_1^{\text{ZDC-SMD}}; Y\}$ ($\text{Res}\{\Psi_1^{\text{ZDC-SMD}}; X\}$) was systematically higher (lower) by about 30% than the expected resolution when the resolutions were calculated with $k = 1$ in Eq. (8). The difference between $\text{Res}\{\Psi_1^{\text{ZDC-SMD}}; X\}$ and $\text{Res}\{\Psi_1^{\text{ZDC-SMD}}; Y\}$ for the two-subevents method is attributed to the non-uniform acceptance between horizontal (x) and vertical (y) directions of the ZDC-SMD. Those resolutions of the ZDC-SMD were consistent with each other using $k = 2$. For $k = 2$, the non-uniform acceptance in the azimuthal directions cancels out

since $\text{Res}\{\Psi_1^{\text{ZDC-SMD}}; X, Y\}$ contain both $\langle \cos(\Psi) \rangle$ and $\langle \sin(\Psi) \rangle$ terms. Thus, $\text{Res}\{\Psi_1^{\text{ZDC-SMD}}; X, Y\}$ should be the same and consistent with that from the expected resolution.

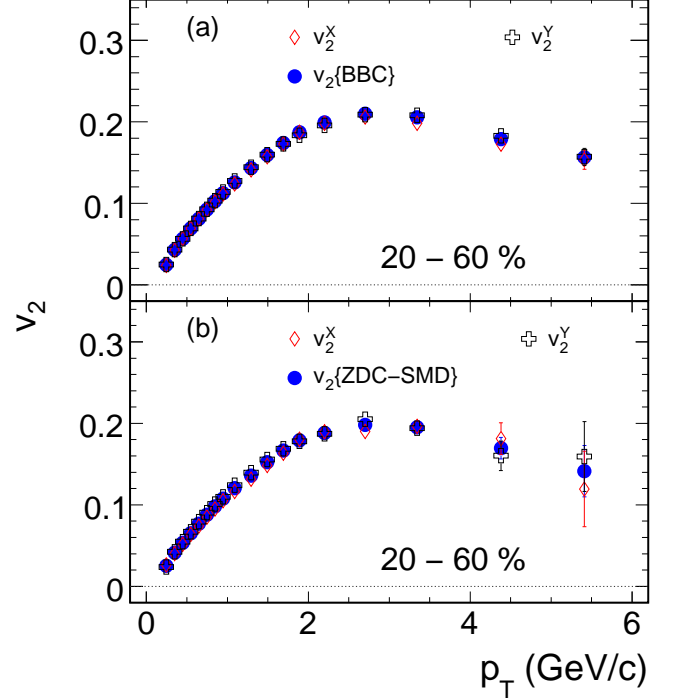


FIG. 16: (a) Comparison of v_2^X (open diamonds) and v_2^Y (open crosses) with the total v_2 (filled circles) for the BBC event plane as a function of p_T for the centrality bin 20–60%. $\text{Res}\{\Psi_n; X\}$ and $\text{Res}\{\Psi_n; Y\}$ are calculated by the combination of the ZDC-SMD, BBC and CNT event planes. Acceptance corrections are included into v_2^X and v_2^Y . Error bars denote statistical errors. (b) The same comparison for the ZDC-SMD event plane.

The comparison of v_2^X and v_2^Y with v_2 with respect to the BBC and ZDC-SMD event planes is shown in Fig. 16. The maximum difference of v_2^X and v_2^Y relative to $v_2\{\text{BBC}\}$ is about 2% for the centrality range 20–60% and is independent of centrality. Systematic uncertainties are evaluated by scaling the maximum difference by $2/\sqrt{12}$. The same comparison is also made for $v_2\{\text{ZDC-SMD}\}$ as shown in the bottom panel in Fig. 16. The systematic errors range from 1–25% and in this case strongly depend on the centrality, as well as on the corrections by the different event plane resolutions. v_2^X and v_2^Y are ~ 10 –25% different from $v_2\{\text{ZDC-SMD}\}$ in the 0–20% centrality bin due to the very low resolution. This systematic uncertainty is denoted as “Acceptance effect on event planes” in Table III.

B. Cumulant method

The potential sources of systematic errors on the cumulant measurements are detailed below.

1. Fixed multiplicity cut

Following Ref. [42] a fixed multiplicity is used to reconstruct the integrated flow to avoid introducing additional errors arising from a fluctuating multiplicity. In our analysis the systematic errors were estimated by varying the fixed multiplicity cut used for the reconstruction of the integrated flow and studying its effect on the differential flow values.

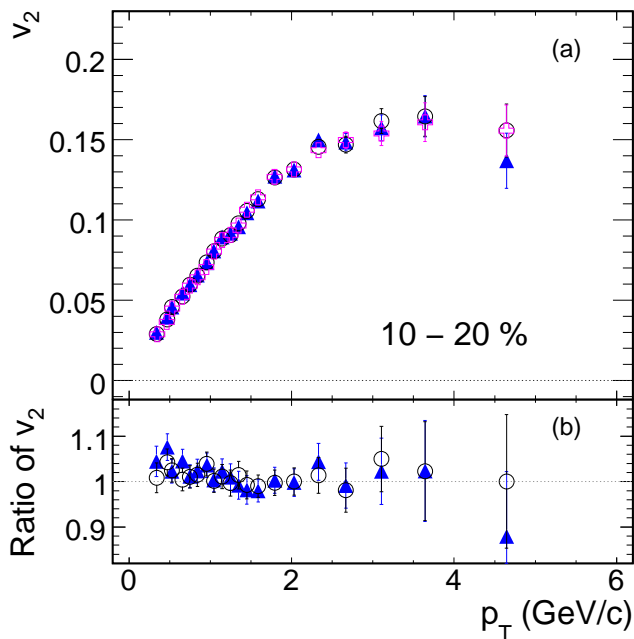


FIG. 17: (a) $v_2\{2\}$ as a function of p_T for centrality 10–20% in Au+Au collisions at $\sqrt{s_{NN}} = 200$ GeV for different fixed multiplicity cuts, corresponding to 60% (filled triangles), 70% (open circles) and 80% (open crosses) of the mean multiplicity. (b) The ratio of $v_2(p_T)$ for the two lowest multiplicity cuts to $v_2(p_T)$ for 80% of the mean multiplicity.

Figure 17(a) shows the variation of v_2 with p_T for integral multiplicity cuts equal to 60%, 70%, and 80% of the mean multiplicity for the centrality bin 20–40%. The ratio of the differential v_2 values, shown in Fig. 17(b), is used to estimate the systematic error on our measurements, which is $\sim 5\%$.

2. p_T range for integrated flow

In order to assess the influence of the p_T range used to estimate the integrated flow on the differential flow, we chose different p_T ranges over which the integral particles were selected. Differential v_2 results were obtained for three p_T ranges: 0.25 - 2.0 GeV/c, 0.25 - 1.5 GeV/c and 0.3 - 1.5 GeV/c. The systematic error from this source is estimated to be 3–8% depending on centrality and p_T .

3. Background contribution

The procedures followed for studying the background contribution to $v_2\{2\}$ were the same as for the event plane method. After background subtraction the systematic error is calculated by determining the difference between the v_2 obtained from using 2σ and 3σ association cuts. We determined that the overall systematic error due to these differences is 6–10% depending on p_T and centrality.

V. RESULTS

A. p_T dependence of v_2

The p_T dependence of v_2 has been instrumental in revealing the hydrodynamic properties of the matter formed at RHIC [19, 21]. In this context, it is important to compare the p_T dependence of v_2 from different methods to establish the robustness of our v_2 measurements. This comparison is displayed in Fig. 18 which shows the differential charged hadron v_2 as a function of p_T from the event plane and cumulant methods for different centrality bins in the range 0–60% in Au+Au at $\sqrt{s_{NN}} = 200$ GeV. $v_2\{2\}$ increases up to $p_T \approx 3$ GeV/c and saturates at 0.1–0.25, depending on centrality, for higher p_T . On the other hand, $v_2\{\text{BBC}\}$ and $v_2\{\text{ZDC-SMD}\}$ reach their maximum value at $p_T \approx 3$ GeV/c, and decrease for higher p_T .

The differences between $v_2\{\text{BBC}\}$ and $v_2\{\text{ZDC-SMD}\}$ are independent of p_T within systematic errors in the measured centrality range. $v_2\{\text{ZDC-SMD}\}$ is consistent with $v_2\{\text{BBC}\}$ within systematic errors in the 0–40% centrality range, but is ~ 10 –20% smaller than $v_2\{\text{BBC}\}$ in the 40–60% centrality range. These results could indicate that the influence of non-flow effects on $v_2\{\text{BBC}\}$ is small and within the systematic errors, because non-flow effects are not expected to influence $v_2\{\text{ZDC-SMD}\}$. The difference between $v_2\{\text{BBC}\}$ and $v_2\{\text{ZDC-SMD}\}$ in peripheral collisions could be attributed to non-flow contributions that might be proportionally larger in more peripheral collisions.

The cumulant and event plane v_2 agree well within systematic uncertainties in the centrality range 0–40%. In more peripheral collisions, there may be some differences developing above $p_T \simeq 4$ GeV/c. Correlations be-

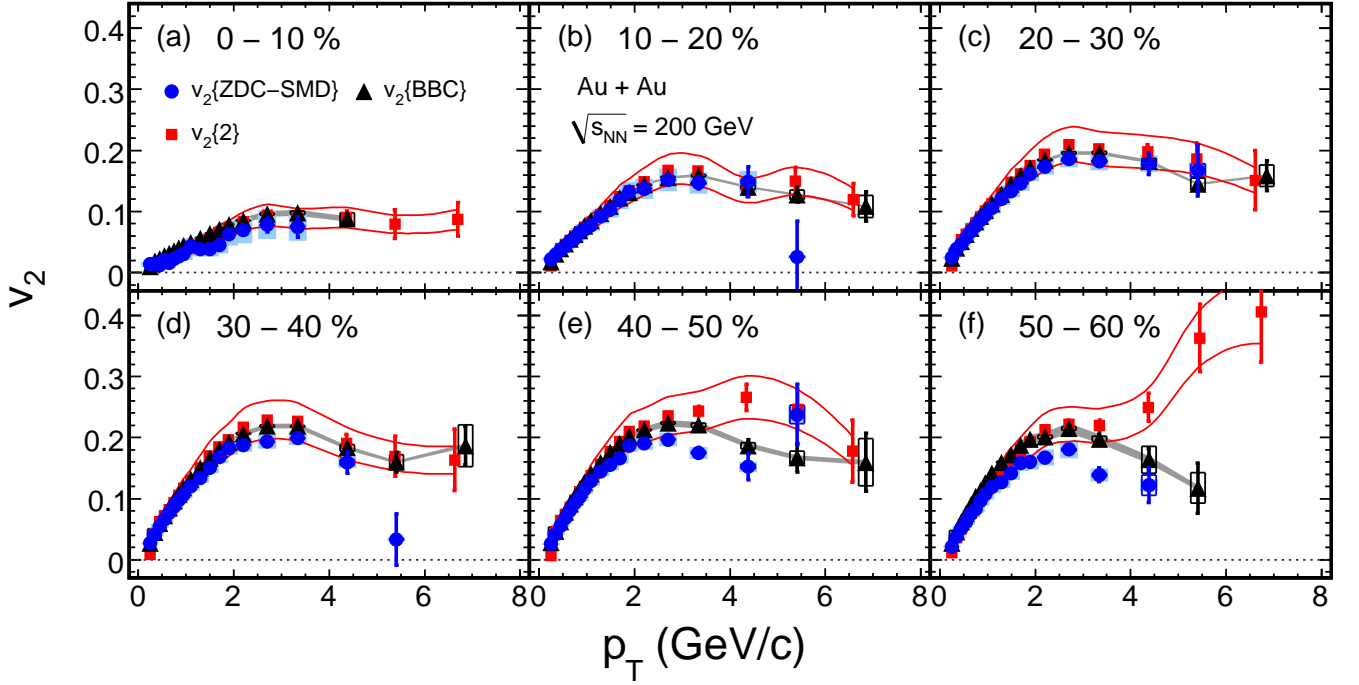


FIG. 18: Charged hadron $v_2(p_T)$ in Au+Au collisions at $\sqrt{s_{NN}} = 200$ GeV from the two-particle cumulant method (filled squares), the BBC event plane (filled triangles) and the ZDC-SMD event plane (filled circles) for centrality (a) 0–10%, (b) 10–20%, (c) 20–30%, (d) 30–40%, (e) 40–50%, and (f) 50–60%. Error bars denote statistical errors. The type B systematic uncertainties are represented by the open boxes for the $v_2\{\text{BBC}\}$ and $v_2\{\text{ZDC-SMD}\}$, and by the solid lines for the $v_2\{2\}$. The gray bands and blue boxes represent the type C systematic uncertainties on the $v_2\{\text{BBC}\}$ and $v_2\{\text{ZDC-SMD}\}$, respectively.

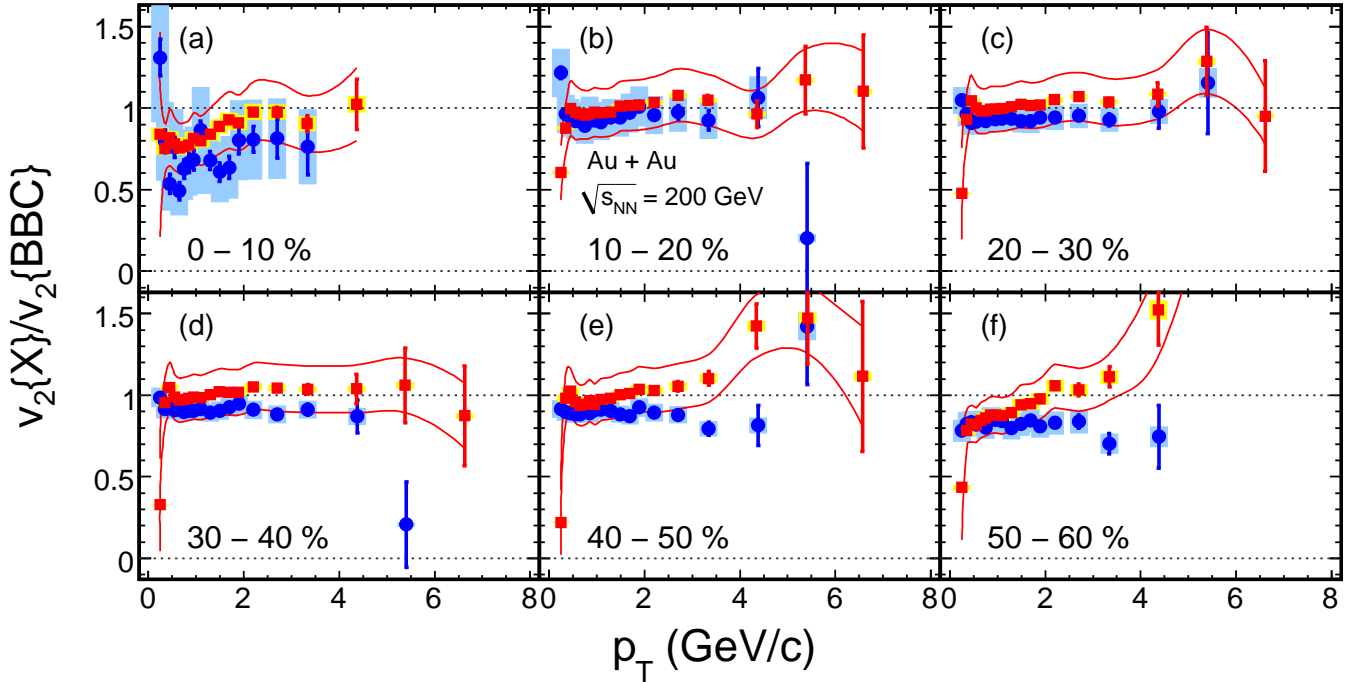


FIG. 19: The ratio of v_2 to $v_2\{\text{BBC}\}$ as a function of p_T for six centrality bins over the range 0–60% in Au+Au collisions at $\sqrt{s_{NN}} = 200$ GeV. Data symbols are the same as in the Fig. 18. Error bars denote statistical errors. The solid red lines represent the type B systematic errors on the $v_2\{2\}$. The blue and yellow bands represent type C systematic uncertainties on $v_2\{\text{ZDC-SMD}\}$ and $v_2\{2\}$.

tween particles from jets affect the cumulant results, but have less influence on $v_2\{\text{BBC}\}$, as explained in Ref. [29],

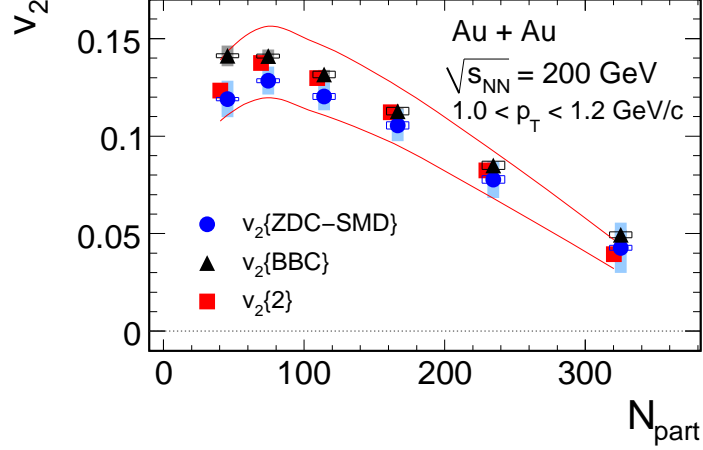


FIG. 20: Comparison of charged hadron v_2 at $1 < p_T < 1.2$ GeV/ c as a function of N_{part} for $v_2\{\text{BBC}\}$ (filled triangles), $v_2\{\text{ZDC-SMD}\}$ (filled circles) and $v_2\{2\}$ (filled squares) in Au+Au at $\sqrt{s_{\text{NN}}} = 200$ GeV. The error bars represent statistical errors. The open boxes represent type B systematic uncertainties on $v_2\{\text{BBC}\}$ and $v_2\{\text{ZDC-SMD}\}$. Type B systematic uncertainties on $v_2\{2\}$ are represented by solid red lines. The gray and blue bands represent type C systematic errors on $v_2\{\text{BBC}\}$ and $v_2\{\text{ZDC-SMD}\}$, respectively. $v_2\{2\}$ values are shifted in the x-axis to improve the plot.

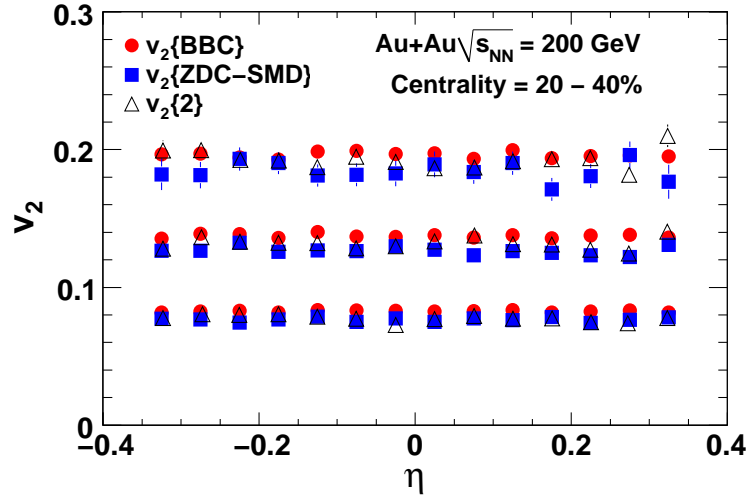


FIG. 21: Anisotropy parameter v_2 as a function of pseudorapidity within the PHENIX central arms using event planes from the BBC (filled circles), ZDC-SMD (filled squares), and from the two-particle cumulant method (open triangles) for centrality 20–40%. The results are shown for three p_T bins, which are from top to bottom: 2.0–3.0, 1.2–1.4 and 0.6–0.8 GeV/ c . Only statistical errors are shown.

where it was shown that the smaller the rapidity gap between the leading particle from a jet and the event plane, the greater the v_2 of the leading particle of the jet.

In order to illustrate more clearly the differences between the different methods, Fig. 19 shows the ratio of $v_2\{\text{ZDC-SMD}\}$ and $v_2\{2\}$ to $v_2\{\text{BBC}\}$. The results from the three methods are comparable in magnitude within systematic errors, except for the central and peripheral bins where the largest deviations occur. In addition, $v_2\{2\}$ and $v_2\{\text{ZDC-SMD}\}$ show different behaviors at $p_T > 3$ GeV/ c , with $v_2\{2\}$ being larger, and $v_2\{\text{ZDC-SMD}\}$,

smaller than $v_2\{\text{BBC}\}$.

B. Centrality dependence of v_2

Figure 20 shows the N_{part} dependence of v_2 from different methods for charged hadrons in the range $1.0 < p_T < 1.2$ GeV/ c . v_2 is observed to increase with decreasing N_{part} and then decrease slightly for $N_{\text{part}} \lesssim 75$. Note that v_2 values obtained with the different methods agree well within systematic errors for all centralities. This is

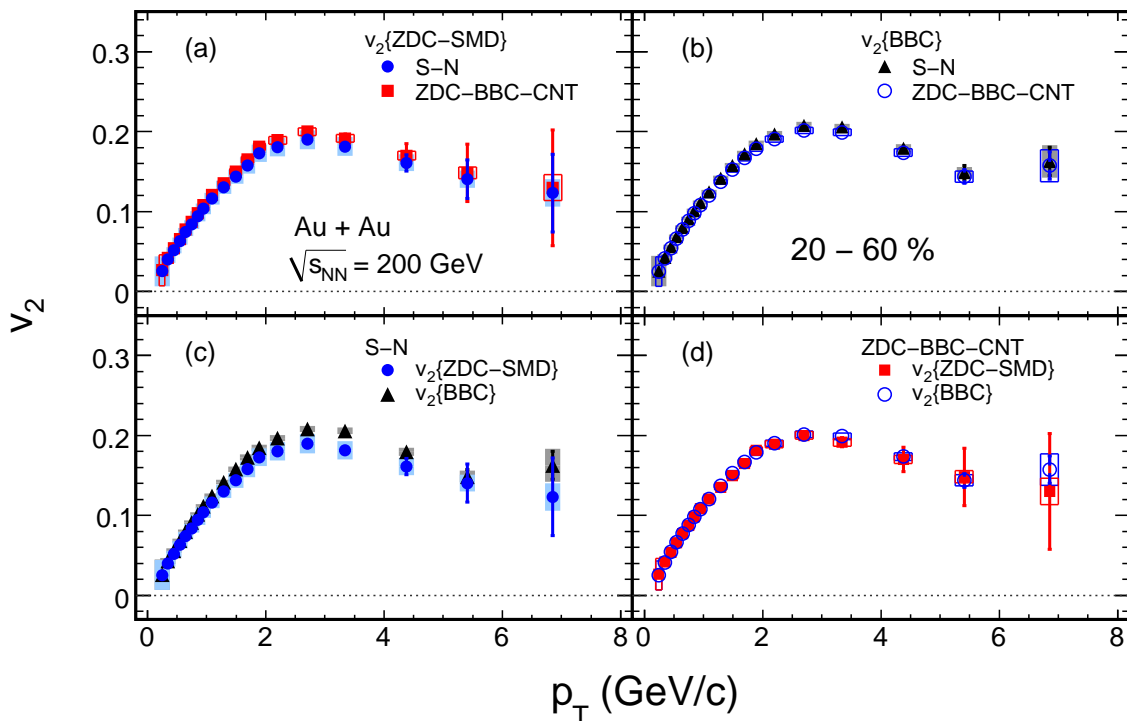


FIG. 22: (a) Comparison of the $v_2\{\text{ZDC-SMD}\}$ from the S-N (filled circles) and ZDC-BBC-CNT subevents (filled squares) as a function of p_T in the 20–60% centrality range. (b) The same comparison as (a) for the $v_2\{\text{BBC}\}$, where filled triangles and open circles represent the v_2 from the S-N and ZDC-BBC-CNT subevents, respectively. (c) Comparison of v_2 between BBC (filled triangles) and ZDC-SMD event planes (filled circles) from the S-N subevent as a function of p_T in centrality 20–60%. (d) The same comparison as (c) from the ZDC-BBC-CNT subevent, where filled squares and open circles represent the $v_2\{\text{ZDC-SMD}\}$ and $v_2\{\text{BBC}\}$, respectively. Error bars denote statistical errors. Open boxes and shaded bands describe the quadratic sum of type B and C systematic uncertainties from the S-N and ZDC-BBC-CNT subevents, respectively.

p_T dependent, as shown in Fig. 18.

C. Pseudorapidity dependence of v_2

Figure 21 compares the pseudorapidity dependence of the v_2 of charged hadrons within the η range (± 0.35) of the PHENIX central arms for different p_T selections. It can be observed that v_2 is constant over the η coverage of the PHENIX detector and the constancy does not depend on p_T . This is not the case when the v_2 is measured far from midrapidity where the PHOBOS and STAR collaborations observe a drop in v_2 for $|\eta| > 1.0$ [47, 48].

VI. DISCUSSION

A. Effect of CNT event plane resolution

Figure 22 shows the comparison of $v_2\{\text{ZDC-SMD}\}$ and $v_2\{\text{BBC}\}$ as a function of p_T corrected either by the resolution from South-North correlations from the same detectors or by the resolution from ZDC-SMD-CNT correlations in the 20–60% centrality bin. Fig-

ures 22(a) and (b) compare the v_2 obtained by using two different corrections from the South-North and ZDC-BBC-CNT subevents for the BBC (a) and ZDC-SMD event planes (b). The v_2 from the South-North subevent is consistent with that from the ZDC-BBC-CNT subevent, within systematic uncertainties. The small difference between South-North and ZDC-BBC-CNT subevents is attributed to the difference between the event plane resolution, as shown in Fig. 4. Figures 22(c) and (d) compare $v_2\{\text{ZDC-SMD}\}$ with $v_2\{\text{BBC}\}$ for the South-North (c) and ZDC-BBC-CNT subevent (d). The data points in Fig. 22(c) and (d) are the same as in Fig. 22(a) and (b). Figure 22(c) shows that $v_2\{\text{ZDC-SMD}\}$ is about 10% smaller than $v_2\{\text{BBC}\}$ for the South-North subevent. The ratio of $v_2\{\text{ZDC-SMD}\}$ to $v_2\{\text{BBC}\}$ is found to be independent of p_T except for $6 < p_T < 8$ GeV/c. If jets are the dominant source of non-flow, one expects its contribution to v_2 to become larger at higher p_T . The constant ratio suggests that the non-flow contribution from jets is small and v_2 fluctuations may affect $v_2\{\text{BBC}\}$ below $p_T \approx 6$ GeV/c since the effect of fluctuations is expected to be independent of p_T . $v_2\{\text{ZDC-SMD}\}$ agrees with $v_2\{\text{BBC}\}$ within systematic uncertainties for the ZDC-BBC-CNT subevent as shown in Fig. 22(d). The event plane resolution from the ZDC-

BBC-CNT subevents includes the effect of non-flow contributions and v_2 fluctuations since the CNT and BBC event planes are sensitive to both effects, though non-flow effects especially from jets could be negligible in the BBC event plane, as discussed earlier. The consistency between v_2 from the ZDC-SMD and BBC event planes may suggest that $v_2\{\text{ZDC-SMD}\}$ becomes sensitive to v_2 fluctuations by the inclusion of the BBC and CNT event planes to estimate the resolution.

B. Comparison with other experiments

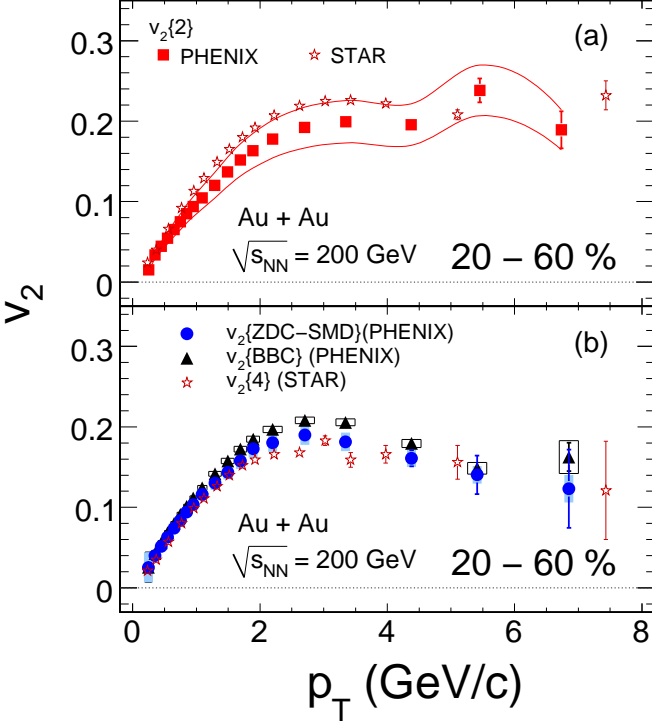


FIG. 23: (a) Comparison of charged hadron $v_2\{2\}$ between PHENIX (filled squares) and STAR experiments (open stars) as a function of p_T in centrality 20–60%. Solid lines represent the quadratic sum of type B and C systematic errors on the PHENIX $v_2\{2\}$. (b) Comparison of charged hadron v_2 from four-particle cumulant $v_2\{4\}$ at STAR (open stars) with the PHENIX $v_2\{\text{BBC}\}$ (filled triangles) and $v_2\{\text{ZDC-SMD}\}$ (filled circles) as a function of p_T in centrality 20–60%. Open boxes and shaded bands represent the quadratic sum of type B and C systematic errors on the $v_2\{\text{BBC}\}$ and $v_2\{\text{ZDC-SMD}\}$, respectively. STAR results are taken from Ref. [49]. Systematic errors on the STAR v_2 are not plotted, see text for more details.

It is instructive to compare measurements made by different experiments at RHIC. Figure 23 shows a comparison of the p_T dependence of charged hadron v_2 in the 20–60% centrality range between PHENIX and STAR experiments [49]. The relative systematic errors on the STAR $v_2\{2\}$ and $v_2\{4\}$ measurements range up to 10% for p_T

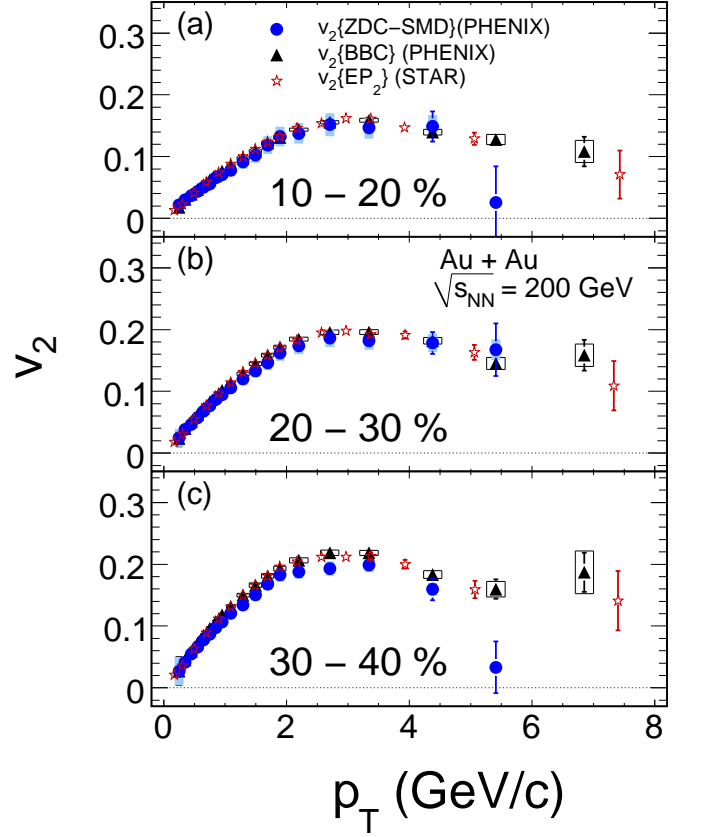


FIG. 24: Comparison of the PHENIX $v_2\{\text{BBC}\}$ (filled triangles) and $v_2\{\text{ZDC-SMD}\}$ (filled circles) with the STAR v_2 from modified event plane method (open stars) for charged hadrons [47] as a function of p_T in centrality (a) 10–20%, (b) 20–30%, and (c) 30–40%. Open boxes and shaded bands represent the quadratic sum of type B and C systematic errors on $v_2\{\text{BBC}\}$ and $v_2\{\text{ZDC-SMD}\}$, respectively.

< 1 GeV/c, with the lowest p_T bin having the largest error $\sim 10\%$, while they are of the order of 1% above 1 GeV/c [49]. The $v_2\{2\}$ from PHENIX is lower than that from STAR, but they are comparable within systematic uncertainties, as shown in Fig. 23(a). Figure 23(b) compares $v_2\{\text{BBC}\}$ and $v_2\{\text{ZDC-SMD}\}$ with $v_2\{4\}$, obtained from four particle cumulants, as measured in STAR. For $p_T > 2$ GeV/c, the STAR $v_2\{4\}$ is systematically smaller than the PHENIX event plane v_2 , while $v_2\{\text{ZDC-SMD}\}$ is lower than $v_2\{\text{BBC}\}$. However, the three set of measurements are consistent within systematic errors. The order of v_2 , $v_2\{\text{BBC}\} > v_2\{\text{ZDC-SMD}\} > v_2\{4\}$ could be explained by the effect of flow fluctuations [50, 51] if other non-flow contributions are small.

Figure 24 shows the comparison of our charged hadron v_2 from the BBC and ZDC-SMD event planes to v_2 from a modified event plane method [47], labelled $v_2\{\text{EP}_2\}$, from the STAR experiment for three centrality bins in the range 10–40%. Particles within $|\Delta\eta| < 0.5$ around the highest p_T particle were excluded for the determination of the modified event plane in order to reduce some of

the non-flow effects at high p_T . We find that $v_2\{\text{BBC}\}$ agrees well with $v_2\{\text{EP}_2\}$ over the measured p_T range, whereas $v_2\{\text{ZDC-SMD}\}$ is generally slightly smaller than $v_2\{\text{EP}_2\}$.

VII. SUMMARY

In summary we have presented PHENIX elliptic flow measurements for unidentified charged hadrons from the event plane and the two-particle cumulant methods as a function of p_T and centrality at midrapidity ($|\eta| < 0.35$) in Au+Au collisions at $\sqrt{s_{NN}} = 200$ GeV. The first harmonic ZDC-SMD event plane is used to measure v_2 and is compared to v_2 from the second harmonic BBC event plane in order to understand the possible non-flow contributions as well as the effect of v_2 fluctuations on $v_2\{\text{BBC}\}$.

The comparison between v_2 from two-particle cumulant and event plane methods shows that they agree within systematic errors. However, non-flow effects from jet correlations begin to contribute to the two-particle cumulant v_2 , especially for peripheral collisions and at high p_T .

In contrast, non-flow effects on $v_2\{\text{BBC}\}$ are very small. The measured $v_2\{\text{BBC}\}$ values decrease by about 3% when the central arm event plane is included in the estimate of the BBC reaction plane resolution. This could be due to a partial compensation of the non-flow effects on the measured v_2 , though the results of $v_2\{\text{BBC}\}$ with and without the CNT event plane resolution are consistent within systematic errors. The strongest evidence that non-flow effects on $v_2\{\text{BBC}\}$ are small comes from the observation that $v_2\{\text{ZDC-SMD}\}$ is comparable with $v_2\{\text{BBC}\}$ within systematic uncertainties in the 0–40% centrality range, and are only ~ 5 –10% smaller than $v_2\{\text{BBC}\}$ for the 40–60% centrality bin. The magnitude of this difference could indicate the level at which non-flow effects such as jets or the ridge could impact the measured flow. However, PHOBOS has observed the ridge to be strongest in central collisions[30] where we observe that $v_2\{\text{ZDC-SMD}\}$ is comparable with $v_2\{\text{BBC}\}$. For collisions that are more peripheral than 40% centrality, PHOBOS observes no ridge[30], so it is unlikely that our observation that $v_2\{\text{ZDC-SMD}\}$ is ~ 5 –10% smaller than $v_2\{\text{BBC}\}$ for the 40–60% centrality bin is caused by the ridge. Moreover, the difference between $v_2\{\text{ZDC-SMD}\}$ and $v_2\{\text{BBC}\}$ is independent of p_T in the measured centrality range.

Due to the large pseudorapidity gap between the event plane and the particles detected in the central arms spectrometer, and the first harmonic event plane from directed flow by spectator neutrons, $v_2\{\text{ZDC-SMD}\}$ is considered to provide an unbiased measure of the elliptic flow. Within systematic uncertainties the measured $v_2\{\text{ZDC-SMD}\}$ from PHENIX is consistent with v_2 from the four particle cumulant method measured by the STAR experiment in the 20–60% centrality bin, and

is also consistent with the STAR v_2 from a modified event plane method in 10–40% centrality bins. These comparisons (1) further demonstrate the validity of the $v_2\{\text{ZDC-SMD}\}$, because both STAR results aim to minimize the non-flow effects, (2) reinforce the robustness of the BBC event plane method at RHIC, and (3) confirm previous studies of the influence of jets on the measured v_2 for different rapidity gaps. Hence, $v_2\{\text{BBC}\}$ can be used to infer constraints on the hydrodynamic behavior of heavy-ion collisions at RHIC.

Acknowledgements

We thank the staff of the Collider-Accelerator and Physics Departments at Brookhaven National Laboratory and the staff of the other PHENIX participating institutions for their vital contributions. We acknowledge support from the Office of Nuclear Physics in the Office of Science of the Department of Energy, the National Science Foundation, Abilene Christian University Research Council, Research Foundation of SUNY, and Dean of the College of Arts and Sciences, Vanderbilt University (U.S.A), Ministry of Education, Culture, Sports, Science, and Technology and the Japan Society for the Promotion of Science (Japan), Conselho Nacional de Desenvolvimento Científico e Tecnológico and Fundação de Amparo à Pesquisa do Estado de São Paulo (Brazil), Natural Science Foundation of China (People's Republic of China), Centre National de la Recherche Scientifique, Commissariat à l'Énergie Atomique, and Institut National de Physique Nucléaire et de Physique des Particules (France), Ministry of Industry, Science and Technologies, Bundesministerium für Bildung und Forschung, Deutscher Akademischer Austausch Dienst, and Alexander von Humboldt Stiftung (Germany), Hungarian National Science Fund, OTKA (Hungary), Department of Atomic Energy (India), Israel Science Foundation (Israel), Korea Research Foundation and Korea Science and Engineering Foundation (Korea), Ministry of Education and Science, Russia Academy of Sciences, Federal Agency of Atomic Energy (Russia), VR and the Wallenberg Foundation (Sweden), the U.S. Civilian Research and Development Foundation for the Independent States of the Former Soviet Union, the US-Hungarian NSF-OTKA-MTA, and the US-Israel Binational Science Foundation.

APPENDIX: DATA TABLES OF v_2

Tables IV–X show numerical data in the same units as plotted in the figures: p_T (GeV/c), v_2 , type A statistical error σ_{stat} , type B systematic error σ_{syst}^B and type C systematic error σ_{syst}^C .

TABLE IV: $v_2\{2\}$ as a function of p_T in centralities 0–10%, 10–20%, 20–30%, 30–40%, 40–50%, and 50–60%.

Centrality	p_T (GeV/c)	v_2	σ_{stat}	σ_{syst}^B	σ_{syst}^C	Centrality	p_T (GeV/c)	v_2	σ_{stat}	σ_{syst}^B	σ_{syst}^C
0–10%	0.247	0.00859	0.00014	0.00001	0.00000	30–40%	0.250	0.00898	0.00021	0.00001	0.00000
	0.347	0.01406	0.00019	0.00004	0.00000		0.349	0.04323	0.00030	0.00026	0.00000
	0.450	0.01882	0.00023	0.00007	0.00000		0.448	0.06214	0.00036	0.00053	0.00000
	0.547	0.02140	0.00027	0.00009	0.00000		0.548	0.07193	0.00042	0.00071	0.00000
	0.649	0.02395	0.00031	0.00011	0.00000		0.648	0.08243	0.00048	0.00093	0.00000
	0.748	0.02718	0.00036	0.00014	0.00000		0.748	0.09401	0.00055	0.00121	0.00000
	0.847	0.03087	0.00041	0.00018	0.00000		0.848	0.10533	0.00063	0.00153	0.00000
	0.949	0.03605	0.00047	0.00024	0.00000		0.948	0.11678	0.00071	0.00187	0.00000
	1.090	0.03950	0.00041	0.00029	0.00000		1.092	0.12972	0.00063	0.00231	0.00000
	1.291	0.04734	0.00053	0.00042	0.00000		1.291	0.15059	0.00081	0.00312	0.00000
	1.490	0.05633	0.00070	0.00059	0.00000		1.489	0.16955	0.00107	0.00395	0.00000
	1.689	0.06542	0.00095	0.00080	0.00000		1.689	0.18422	0.00147	0.00467	0.00000
	1.890	0.07148	0.00128	0.00096	0.00000		1.891	0.19625	0.00198	0.00529	0.00000
	2.194	0.08352	0.00128	0.00130	0.00000		2.197	0.21718	0.00196	0.00648	0.00000
	2.698	0.09362	0.00249	0.00164	0.00000		2.702	0.22835	0.00369	0.00717	0.00000
	3.329	0.08866	0.00421	0.00147	0.00000		3.338	0.22623	0.00556	0.00704	0.00000
4.365	0.08997	0.01134	0.00151	0.00000	4.360	0.19059	0.01496	0.00499	0.00000		
5.376	0.07933	0.02365	0.00118	0.00000	5.379	0.16931	0.03256	0.00394	0.00000		
6.695	0.08701	0.02720	0.00142	0.00000	6.628	0.16346	0.05010	0.00367	0.00000		
10–20%	0.248	0.01089	0.00013	0.00002	0.00000	40–50%	0.250	0.00625	0.00032	0.00001	0.00000
	0.348	0.02714	0.00018	0.00011	0.00000		0.349	0.04611	0.00044	0.00028	0.00000
	0.449	0.03914	0.00023	0.00023	0.00000		0.448	0.06387	0.00054	0.00054	0.00000
	0.547	0.04592	0.00027	0.00032	0.00000		0.548	0.07455	0.00062	0.00073	0.00000
	0.649	0.05281	0.00030	0.00042	0.00000		0.648	0.08575	0.00072	0.00097	0.00000
	0.748	0.05977	0.00035	0.00054	0.00000		0.748	0.09774	0.00082	0.00126	0.00000
	0.848	0.06637	0.00040	0.00066	0.00000		0.848	0.11126	0.00094	0.00163	0.00000
	0.948	0.07459	0.00045	0.00083	0.00000		0.948	0.11974	0.00108	0.00189	0.00000
	1.092	0.08249	0.00040	0.00102	0.00000		1.092	0.13745	0.00095	0.00249	0.00000
	1.291	0.09506	0.00051	0.00136	0.00000		1.291	0.15672	0.00123	0.00324	0.00000
	1.490	0.10997	0.00067	0.00181	0.00000		1.489	0.17633	0.00166	0.00410	0.00000
	1.689	0.12394	0.00090	0.00230	0.00000		1.689	0.19315	0.00229	0.00492	0.00000
	1.891	0.13378	0.00121	0.00268	0.00000		1.891	0.20965	0.00309	0.00580	0.00000
	2.196	0.14881	0.00121	0.00332	0.00000		2.199	0.21909	0.00304	0.00633	0.00000
	2.699	0.16781	0.00232	0.00422	0.00000		2.701	0.23572	0.00567	0.00733	0.00000
	3.328	0.16669	0.00382	0.00417	0.00000		3.344	0.24331	0.00808	0.00781	0.00000
4.357	0.13468	0.01047	0.00272	0.00000	4.346	0.26575	0.02124	0.00932	0.00000		
5.371	0.14951	0.02244	0.00335	0.00000	5.414	0.24613	0.03288	0.00799	0.00000		
6.587	0.11931	0.02641	0.00214	0.00000	6.566	0.17786	0.05097	0.00417	0.00000		
20–30%	0.249	0.01127	0.00015	0.00002	0.00000	50–60%	0.251	0.01201	0.00052	0.00002	0.00000
	0.349	0.03713	0.00022	0.00019	0.00000		0.349	0.03575	0.00056	0.00016	0.00000
	0.448	0.05370	0.00028	0.00040	0.00000		0.448	0.05111	0.00063	0.00033	0.00000
	0.548	0.06252	0.00032	0.00054	0.00000		0.548	0.06256	0.00071	0.00050	0.00000
	0.648	0.07147	0.00036	0.00070	0.00000		0.648	0.07591	0.00080	0.00073	0.00000
	0.748	0.08144	0.00041	0.00091	0.00000		0.748	0.08903	0.00091	0.00101	0.00000
	0.848	0.09118	0.00047	0.00114	0.00000		0.848	0.09965	0.00103	0.00126	0.00000
	0.948	0.10071	0.00053	0.00139	0.00000		0.948	0.11124	0.00118	0.00157	0.00000
	1.092	0.11227	0.00047	0.00173	0.00000		1.091	0.12340	0.00103	0.00193	0.00000
	1.291	0.12982	0.00060	0.00232	0.00000		1.290	0.14241	0.00133	0.00257	0.00000
	1.489	0.14786	0.00079	0.00301	0.00000		1.489	0.16236	0.00178	0.00334	0.00000
	1.689	0.16113	0.00107	0.00357	0.00000		1.689	0.17737	0.00248	0.00399	0.00000
	1.891	0.17515	0.00145	0.00422	0.00000		1.890	0.19295	0.00337	0.00472	0.00000
	2.196	0.19364	0.00143	0.00515	0.00000		2.198	0.21282	0.00330	0.00575	0.00000
	2.699	0.20931	0.00271	0.00602	0.00000		2.700	0.22201	0.00623	0.00625	0.00000
	3.333	0.20299	0.00430	0.00567	0.00000		3.348	0.21980	0.00917	0.00613	0.00000
4.356	0.19729	0.01175	0.00535	0.00000	4.373	0.24935	0.02292	0.00789	0.00000		
5.383	0.18635	0.02567	0.00477	0.00000	5.452	0.36285	0.05515	0.01671	0.00000		
6.611	0.15079	0.04839	0.00313	0.00000	6.734	0.40554	0.08167	0.02087	0.00000		

TABLE V: $v_2\{2\}$ as a function of p_T in centrality 20–60%.

Centrality $v_2\{\}$	p_T (GeV/c)	v_2	σ_{stat}	σ_{syst}^B	σ_{syst}^C	p_T (GeV/c)	v_2	σ_{stat}	σ_{syst}^B	σ_{syst}^C
20–60% $v_2\{2\}$	0.251	0.00778	0.00011	0.00001	0.00000	1.489	0.14884	0.00058	0.00292	0.00000
	0.349	0.03793	0.00016	0.00019	0.00000	1.689	0.16226	0.00080	0.00347	0.00000
	0.448	0.05476	0.00020	0.00040	0.00000	1.890	0.17456	0.00108	0.00402	0.00000
	0.548	0.06374	0.00023	0.00054	0.00000	2.198	0.19027	0.00106	0.00478	0.00000
	0.648	0.07303	0.00026	0.00070	0.00000	2.700	0.20415	0.00201	0.00550	0.00000
	0.748	0.08283	0.00030	0.00091	0.00000	3.348	0.21363	0.00304	0.00602	0.00000
	0.848	0.09301	0.00034	0.00114	0.00000	4.373	0.19568	0.00653	0.00505	0.00000
	0.948	0.10247	0.00039	0.00139	0.00000	5.452	0.23823	0.01494	0.00749	0.00000
	1.091	0.11444	0.00034	0.00173	0.00000	6.734	0.18915	0.02297	0.00472	0.00000
	1.290	0.13201	0.00044	0.00230	0.00000					

TABLE VI: $v_2\{\text{BBC}\}$ and $v_2\{\text{ZDC-SMD}\}$ from S-N and ZDC-BBC-CNT subevents as a function of p_T in centrality 20–60%.

Centrality $v_2\{\}$	p_T (GeV/c)	S-N subevents				ZDC-BBC-CNT subevents			
		v_2	σ_{stat}	σ_{syst}^B	σ_{syst}^C	v_2	σ_{stat}	σ_{syst}^B	σ_{syst}^C
20–60% $v_2\{\text{BBC}\}$	0.247	0.02569	0.00009	0.00049	0.00001	0.02486	0.00009	0.00045	0.00001
	0.348	0.04271	0.00009	0.00016	0.00003	0.04133	0.00010	0.00015	0.00003
	0.448	0.05587	0.00010	0.00014	0.00006	0.05407	0.00012	0.00013	0.00005
	0.548	0.06846	0.00011	0.00015	0.00009	0.06625	0.00013	0.00014	0.00008
	0.648	0.08009	0.00013	0.00015	0.00012	0.07751	0.00015	0.00014	0.00011
	0.748	0.09123	0.00014	0.00016	0.00015	0.08828	0.00017	0.00015	0.00014
	0.848	0.10124	0.00016	0.00019	0.00019	0.09798	0.00019	0.00018	0.00018
	0.948	0.11159	0.00018	0.00017	0.00023	0.10799	0.00021	0.00016	0.00021
	1.092	0.12439	0.00016	0.00018	0.00029	0.12038	0.00020	0.00017	0.00027
	1.292	0.14170	0.00020	0.00019	0.00037	0.13713	0.00025	0.00018	0.00035
	1.492	0.15770	0.00027	0.00027	0.00046	0.15261	0.00031	0.00025	0.00043
	1.692	0.17244	0.00037	0.00027	0.00055	0.16688	0.00040	0.00026	0.00051
	1.892	0.18481	0.00050	0.00030	0.00063	0.17885	0.00052	0.00028	0.00059
	2.200	0.19684	0.00049	0.00029	0.00071	0.19049	0.00052	0.00027	0.00067
	2.703	0.20803	0.00092	0.00025	0.00080	0.20132	0.00092	0.00023	0.00075
	3.343	0.20569	0.00141	0.00039	0.00078	0.19905	0.00138	0.00037	0.00073
4.381	0.17942	0.00371	0.00066	0.00059	0.17363	0.00360	0.00062	0.00056	
5.410	0.14862	0.00877	0.00098	0.00041	0.14382	0.00849	0.00092	0.00038	
6.852	0.16262	0.01770	0.00328	0.00049	0.15738	0.01713	0.00308	0.00046	
20–60% $v_2\{\text{ZDC-SMD}\}$	0.247	0.02532	0.00025	0.00047	0.00004	0.02661	0.00035	0.00052	0.00002
	0.348	0.04002	0.00029	0.00014	0.00010	0.04188	0.00037	0.00015	0.00004
	0.448	0.05165	0.00032	0.00012	0.00017	0.05395	0.00041	0.00013	0.00007
	0.548	0.06296	0.00036	0.00013	0.00025	0.06567	0.00046	0.00014	0.00010
	0.648	0.07433	0.00041	0.00013	0.00035	0.07746	0.00051	0.00014	0.00014
	0.748	0.08377	0.00046	0.00013	0.00044	0.08730	0.00057	0.00015	0.00017
	0.848	0.09429	0.00052	0.00017	0.00056	0.09827	0.00065	0.00018	0.00022
	0.948	0.10365	0.00059	0.00015	0.00067	0.10808	0.00074	0.00016	0.00027
	1.092	0.11617	0.00053	0.00016	0.00085	0.12065	0.00063	0.00017	0.00033
	1.292	0.13006	0.00066	0.00016	0.00106	0.13535	0.00081	0.00018	0.00042
	1.492	0.14367	0.00086	0.00023	0.00129	0.14994	0.00109	0.00024	0.00052
	1.692	0.15763	0.00115	0.00023	0.00156	0.16504	0.00150	0.00025	0.00062
	1.892	0.17281	0.00151	0.00026	0.00187	0.18136	0.00203	0.00029	0.00075
	2.200	0.18031	0.00149	0.00024	0.00204	0.18912	0.00200	0.00026	0.00082
	2.703	0.18983	0.00263	0.00021	0.00226	0.19998	0.00375	0.00023	0.00092
	3.343	0.18147	0.00393	0.00030	0.00206	0.19147	0.00576	0.00034	0.00084
4.381	0.16102	0.01018	0.00053	0.00162	0.17005	0.01517	0.00059	0.00066	
5.410	0.14043	0.02402	0.00088	0.00124	0.14833	0.03585	0.00098	0.00050	
6.852	0.12310	0.04849	0.00188	0.00095	0.13003	0.07240	0.00210	0.00039	

TABLE VII: $v_2\{\text{BBC}\}$ from S-N and ZDC-BBC-CNT subevents as a function of p_T in centrality 0–10%, 10–20%, and 20–30%.

Centrality $v_2\{\}$	p_T (GeV/ c)	S-N subevents				ZDC-BBC-CNT subevents			
		v_2	σ_{stat}	σ_{syst}^B	σ_{syst}^C	v_2	σ_{stat}	σ_{syst}^B	σ_{syst}^C
0–10% $v_2\{\text{BBC}\}$	0.247	0.01025	0.00012	0.00008	0.00001	0.00966	0.00016	0.00007	0.00000
	0.348	0.01868	0.00014	0.00003	0.00002	0.01762	0.00025	0.00003	0.00002
	0.448	0.02300	0.00016	0.00005	0.00003	0.02169	0.00030	0.00005	0.00002
	0.548	0.02741	0.00018	0.00007	0.00004	0.02586	0.00035	0.00006	0.00003
	0.648	0.03174	0.00020	0.00007	0.00005	0.02993	0.00041	0.00006	0.00005
	0.748	0.03570	0.00023	0.00007	0.00006	0.03367	0.00046	0.00006	0.00006
	0.848	0.03990	0.00026	0.00007	0.00008	0.03763	0.00051	0.00006	0.00007
	0.948	0.04428	0.00029	0.00008	0.00010	0.04176	0.00057	0.00007	0.00009
	1.092	0.04941	0.00025	0.00008	0.00012	0.04660	0.00061	0.00007	0.00011
	1.292	0.05631	0.00032	0.00008	0.00016	0.05310	0.00070	0.00007	0.00014
	1.492	0.06349	0.00042	0.00008	0.00020	0.05988	0.00082	0.00007	0.00018
	1.692	0.07065	0.00058	0.00012	0.00025	0.06663	0.00096	0.00010	0.00022
	1.892	0.07859	0.00078	0.00011	0.00031	0.07412	0.00115	0.00010	0.00028
	2.200	0.08557	0.00078	0.00009	0.00037	0.08070	0.00121	0.00008	0.00033
	2.703	0.09598	0.00151	0.00015	0.00046	0.09052	0.00179	0.00014	0.00041
	3.343	0.09806	0.00245	0.00031	0.00049	0.09249	0.00257	0.00028	0.00043
4.381	0.08795	0.00699	0.00089	0.00039	0.08295	0.00667	0.00079	0.00035	
5.410	–	–	–	–	–	–	–	–	
6.852	–	–	–	–	–	–	–	–	
10–20% $v_2\{\text{BBC}\}$	0.247	0.01804	0.00010	0.00008	0.00000	0.01754	0.00011	0.00007	0.00000
	0.348	0.03095	0.00011	0.00008	0.00001	0.03008	0.00015	0.00008	0.00001
	0.448	0.03927	0.00012	0.00012	0.00002	0.03816	0.00018	0.00011	0.00002
	0.548	0.04714	0.00014	0.00018	0.00003	0.04582	0.00020	0.00017	0.00003
	0.648	0.05480	0.00015	0.00016	0.00004	0.05326	0.00023	0.00015	0.00004
	0.748	0.06236	0.00017	0.00016	0.00006	0.06060	0.00026	0.00015	0.00005
	0.848	0.06895	0.00019	0.00016	0.00007	0.06701	0.00029	0.00015	0.00006
	0.948	0.07647	0.00022	0.00017	0.00008	0.07432	0.00033	0.00016	0.00008
	1.092	0.08498	0.00019	0.00018	0.00010	0.08259	0.00033	0.00017	0.00010
	1.292	0.09731	0.00024	0.00018	0.00014	0.09457	0.00040	0.00017	0.00013
	1.492	0.10883	0.00032	0.00022	0.00017	0.10576	0.00047	0.00021	0.00016
	1.692	0.12204	0.00044	0.00021	0.00021	0.11860	0.00058	0.00020	0.00020
	1.892	0.13129	0.00059	0.00029	0.00025	0.12760	0.00072	0.00027	0.00023
	2.200	0.14375	0.00058	0.00021	0.00030	0.13970	0.00074	0.00020	0.00028
	2.703	0.15569	0.00112	0.00023	0.00035	0.15130	0.00120	0.00022	0.00033
	3.343	0.15885	0.00177	0.00033	0.00037	0.15437	0.00180	0.00031	0.00034
4.381	0.13970	0.00491	0.00056	0.00028	0.13577	0.00480	0.00053	0.00027	
5.410	0.12763	0.01194	0.00101	0.00024	0.12403	0.01161	0.00095	0.00022	
6.852	0.10820	0.02401	0.00193	0.00017	0.10515	0.02334	0.00183	0.00016	
20–30% $v_2\{\text{BBC}\}$	0.247	0.02367	0.00011	0.00032	0.00001	0.02303	0.00012	0.00030	0.00001
	0.348	0.03981	0.00012	0.00014	0.00002	0.03874	0.00015	0.00014	0.00002
	0.448	0.05138	0.00014	0.00016	0.00004	0.04999	0.00017	0.00015	0.00004
	0.548	0.06250	0.00015	0.00019	0.00006	0.06081	0.00020	0.00018	0.00005
	0.648	0.07276	0.00017	0.00020	0.00008	0.07080	0.00023	0.00019	0.00007
	0.748	0.08298	0.00019	0.00018	0.00010	0.08075	0.00026	0.00017	0.00010
	0.848	0.09184	0.00022	0.00020	0.00012	0.08937	0.00029	0.00019	0.00012
	0.948	0.10139	0.00024	0.00020	0.00015	0.09866	0.00032	0.00019	0.00014
	1.092	0.11279	0.00021	0.00022	0.00019	0.10976	0.00032	0.00021	0.00018
	1.292	0.12862	0.00027	0.00023	0.00024	0.12516	0.00038	0.00022	0.00023
	1.492	0.14459	0.00036	0.00029	0.00031	0.14070	0.00046	0.00027	0.00029
	1.692	0.15864	0.00049	0.00030	0.00037	0.15437	0.00058	0.00029	0.00035
	1.892	0.17169	0.00066	0.00032	0.00043	0.16707	0.00074	0.00030	0.00041
	2.200	0.18437	0.00065	0.00032	0.00050	0.17941	0.00075	0.00030	0.00047
	2.703	0.19554	0.00123	0.00042	0.00056	0.19028	0.00127	0.00039	0.00053
	3.343	0.19585	0.00192	0.00048	0.00056	0.19058	0.00192	0.00046	0.00053
4.381	0.18189	0.00521	0.00088	0.00049	0.17700	0.00509	0.00083	0.00046	
5.410	0.14502	0.01244	0.00138	0.00031	0.14112	0.01211	0.00131	0.00029	
6.852	0.15856	0.02490	0.00286	0.00037	0.15430	0.02423	0.00271	0.00035	

-
- [1] I. Arsene et al. (BRAHMS), Nucl. Phys. **A757**, 1 (2005).
- [2] K. Adcox et al. (PHENIX), Nucl. Phys. **A757**, 184 (2005).
- [3] B. B. Back et al. (PHOBOS), Nucl. Phys. **A757**, 28 (2005).
- [4] J. Adams et al. (STAR), Nucl. Phys. **A757**, 102 (2005).
- [5] M. Gyulassy and L. McLerran, Nucl. Phys. **A750**, 30 (2005).
- [6] B. Muller, nucl-th/0404015.
- [7] E. V. Shuryak, Nucl. Phys. **A750**, 64 (2005).
- [8] J.-Y. Ollitrault, Phys. Rev. D **46**, 229 (1992).
- [9] P. F. Kolb, U. W. Heinz, P. Huovinen, K. J. Eskola, and K. Tuominen, Nucl. Phys. **A696**, 197 (2001).
- [10] T. Hirano and Y. Nara, Nucl. Phys. **A743**, 305 (2004).
- [11] N. N. Ajitanand (PHENIX), Nucl. Phys. **A715**, 765 (2003).
- [12] M. Chiu (PHENIX), Nucl. Phys. **A715**, 761 (2003).
- [13] C. Adler et al. (STAR), Phys. Rev. Lett. **90**, 082302 (2003).
- [14] S. S. Adler et al. (PHENIX), Phys. Rev. C **71**, 051902 (2005).
- [15] J. Adams et al. (STAR), Phys. Rev. Lett. **95**, 152301 (2005).
- [16] S. S. Adler et al. (PHENIX), Phys. Rev. Lett. **97**, 052301 (2006).
- [17] A. Adare et al. (PHENIX), Phys. Rev. C **78**, 014901 (2008).
- [18] M. Bleicher and H. Stoecker, Phys. Lett. **B526**, 309 (2002).
- [19] S. S. Adler et al. (PHENIX), Phys. Rev. Lett. **91**, 182301 (2003).
- [20] Z. Xu, C. Greiner, and H. Stoecker, J. Phys. **G35**, 104016 (2008).
- [21] J. Adams et al. (STAR), Phys. Rev. Lett. **92**, 052302 (2004).
- [22] A. Adare et al. (PHENIX), Phys. Rev. Lett. **98**, 162301 (2007).
- [23] S. Huang (PHENIX), J. Phys. **G35**, 104105 (2008).
- [24] D. Molnár and S. A. Voloshin, Phys. Rev. Lett. **91**, 092301 (2003).
- [25] R. J. Fries, B. Müller, C. Nonaka, and S. A. Bass, Phys. Rev. C **68**, 044902 (2003).
- [26] V. Greco, C. M. Ko, and P. Lévai, Phys. Rev. C **68**, 034904 (2003).
- [27] A. Shor, Phys. Rev. Lett. **54**, 1122 (1985).
- [28] A. M. Poskanzer and S. A. Voloshin, Phys. Rev. C **58**, 1671 (1998).
- [29] J. Jia (PHENIX), Nucl. Phys. **A783**, 501 (2007).
- [30] B. Alver et al., arXiv:0903.2811 [nucl-ex].
- [31] P. Sorensen (STAR), J. Phys. **G35**, 104102 (2008).
- [32] J.-Y. Ollitrault, A. M. Poskanzer, and S. A. Voloshin, arXiv:0904.2315 [nucl-ex].
- [33] K. Adcox et al. (PHENIX), Nucl. Instrum. Meth. **A499**, 469 (2003).
- [34] M. Allen et al. (PHENIX), Nucl. Instrum. Meth. **A499**, 549 (2003).
- [35] C. Adler et al., Nucl. Instrum. Meth. **A499**, 433 (2003).
- [36] M. L. Miller, K. Reygers, S. J. Sanders, and P. Steinberg, Ann. Rev. Nucl. Part. Sci. **57**, 205 (2007).
- [37] R. J. Glauber and G. Matthiae, Nucl. Phys. **B21**, 135 (1970).
- [38] K. Adcox et al. (PHENIX), Phys. Rev. Lett. **86**, 3500 (2001).
- [39] S. S. Adler et al. (PHENIX), Phys. Rev. C **69**, 034910 (2004).
- [40] J. T. Mitchell et al. (PHENIX), Nucl. Instrum. Meth. **A482**, 491 (2002).
- [41] S. S. Adler et al. (PHENIX), Phys. Rev. C **73**, 054903 (2006).
- [42] N. Borghini, P. M. Dinh, and J.-Y. Ollitrault, Phys. Rev. C **64**, 054901 (2001).
- [43] N. Borghini, P. M. Dinh, and J.-Y. Ollitrault (2001).
- [44] C. Alt et al. (NA49), Phys. Rev. C **68**, 034903 (2003).
- [45] C. Adler et al. (STAR), Phys. Rev. C **66**, 034904 (2002).
- [46] I. Selyuzhenkov and S. Voloshin, Phys. Rev. C **77**, 034904 (2008).
- [47] J. Adams et al. (STAR), Phys. Rev. C **72**, 014904 (2005).
- [48] B. Alver et al. (PHOBOS), Phys. Rev. Lett. **98**, 242302 (2007).
- [49] J. Adams et al. (STAR), Phys. Rev. Lett. **93**, 252301 (2004).
- [50] R. S. Bhalerao and J.-Y. Ollitrault, Phys. Lett. **B641**, 260 (2006).
- [51] M. Miller and R. Snellings, nucl-ex/0312008.